UC Berkeley
UC Berkeley Previously Published Works

Title
Theory and Simulation of Metal—Insulator—Semiconductor (MIS) Photoelectrodes

Permalink
https://escholarship.org/uc/item/5mq08362

Journal
ACS Applied Materials & Interfaces, 15(19)

ISSN
1944-8244

Authors
King, Alex J
Weber, Adam Z
Bell, Alexis T

Publication Date
2023-05-17

DOI
10.1021/acsami.2c21114

Copyright Information
This work is made available under the terms of a Creative Commons Attribution-NonCommercial-NoDerivatives License, available at
https://creativecommons.org/licenses/by-nc-nd/4.0/

Peer reviewed

eScholarship.org Powered by the California Digital Library
University of California

Theory and Simulation of Metal-Insulator-Semiconductor (MIS) Photoelectrodes

Alex J. King[1,2], Adam Z. Weber*[2], and Alexis T. Bell*[1,2]

[1] Department of Chemical and Biomolecular Engineering
University of California Berkeley
Berkeley, CA 94720, USA

[2] Liquid Sunlight Alliance
Lawrence Berkeley National Laboratory
Berkeley, CA 94720, USA

*To whom correspondence should be sent: alexbell@berkeley.edu; azweber@lbl.gov

Keywords: photoelectrochemistry, solar-fuels, photoelectrode, metal-insulator-semiconductor, theory, modeling, hydrogen evolution, CO_2 reduction

Abstract

A metal-insulator-semiconductor (MIS) structure is an attractive photoelectrode-catalyst architecture for promoting photoelectrochemical reactions, such as the formation H_2 by proton reduction. The metal catalyzes the generation of H_2 using electrons generated by photon absorption and charge separation in the semiconductor. The insulator layer between the metal and the semiconductor protects the latter element from photo-corrosion and, also, significantly impacts the photovoltage at the metal surface. Understanding how the insulator layer determines the photovoltage and what properties lead to high photovoltages is critical to the development of MIS structures for solar-to-chemical energy conversion. Herein, we present a continuum model for charge-carrier transport from the semiconductor to the metal with an emphasis on mechanisms of charge transport across the insulator. The polarization curves and photovoltages predicted by this model for a Pt/HfO_2/p-Si MIS structure at different HfO_2 thicknesses agree well with experimentally measured data. The simulations reveal how insulator properties (*i.e.*, thickness and band structure) affect band bending near the semiconductor/insulator interface and how tuning them can lead to operation closer to the maximally attainable photovoltage, the flat-band potential. This phenomenon is understood by considering the change in tunneling resistance with insulator properties. The model shows that the best MIS performance is attained with highly symmetric semiconductor/insulator band offsets (*e.g.*, BeO, MgO, SiO_2, HfO_2, or ZrO_2 deposited on Si) and a low to moderate insulator thickness (*e.g.*, between 0.8 and 1.5 nm). Beyond 1.5 nm, the density of filled interfacial trap sites is high and significantly limits the photovoltage and the solar-to-chemical conversion rate. These conclusions are true for photocathodes and photoanodes. This understanding provides critical insight into the phenomena enhancing and limiting photoelectrode performance and how this phenomenon is influenced by insulator properties. The study gives

guidance toward the development of next-generation insulators for MIS structures that achieve high performance.

1. Introduction

Chemical manufacturing has enabled significant population growth and improvement in quality of life; however, its reliance on the combustion of fossil fuels to achieve necessary reaction temperatures and pressures has led to nearly 7% of total anthropogenic CO_2 emissions.[1,2] A promising approach to decouple CO_2 emissions from chemical production is to carry out solar-driven electrochemical synthesis of commodity chemicals (*i.e.*, H_2, NH_3, CO, C_2H_4, C_2H_5OH, O_2, etc.) from H_2O, CO_2, and/or N_2. In this case, the electrochemical potential of electrons is used to drive critical chemical reactions, instead of heat, thereby enabling operation at mild temperatures and pressures.[2] For these systems to have a viable return on investment, it is predicted that the solar-to-chemical (STC) efficiency needs to be $\gtrsim 10$ % (10 mA cm^{-2} at full sun, 100 mW cm^{-2}).[3,4] This STC efficiency has been achieved by connecting an electrochemical (EC) cell to a photovoltaic (PV) device (PV+EC)[5–8] or by integrating the photo-absorber directly into an electrochemical cell, forming a photoelectrochemical (PEC) cell.[6,9–11] However, higher STC efficiency can be reached by connecting PV modules to a PEC cell (PV+PEC) because this combination produces a higher photovoltage to drive the reaction than PV+EC or PEC alone for a fixed solar irradiation,[12,13] thus significantly improving the economic viability of solar-driven electrolysis.[3] The use of PEC cells also has the potential to use light to modify catalytic selectivity through plasmonic effects,[14] induce pH changes with photoacids,[15] and enable internal heat management.[16] Despite these attributes, the design photoelectrodes that exhibit high activity and stability is a current challenge.

Semiconductors (*e.g.*, Si, GaP, GaAs) were the first materials used to absorb visible light and drive electrochemical reactions.[17–19] Although successful in demonstrating STC conversion, the catalytic activity of the bare semiconductor surface is generally poor,[19] and non-oxide

semiconductors suffer from corrosion when submerged in aqueous electrolytes.[18,20,21] To ameliorate these issues, semiconductors with metal catalyst films deposited on their surface (metal-semiconductor systems) have been explored as photoelectrode/catalyst structures.[18,22] The thin metal film helps to protect the semiconductor from corrosion and promotes the kinetics of the desired reactions. Nevertheless, there are several issues with the metal-semiconductor (MS) contact. They typically generate low photovoltages because of high carrier recombination rates in the metal (due to a low interfacial barrier height) and Fermi level pinning.[22–26] Moreover, metal atoms can diffuse into the semiconductor layer and form a mixed MS interlayer that has high ohmic resistance.[27,28]

Insertion of an ultrathin ($\lesssim$ 5 nm), metal-oxide insulating layer between the metal and the semiconductor creates a metal-insulator-semiconductor (MIS) structure that can mitigate all of the aforementioned issues. The insulator introduces a transport barrier that reduces charge recombination in the metal, and it passivates the semiconductor surface, reducing the density of surface trap sites and Fermi level pinning.[23,24,26,28–30] The insulating layer can also block the diffusion of metal atoms and mitigate the growth of the MS interlayer.[31] Furthermore, MIS structures can use porous or nanoparticulate metal catalysts, thereby increasing the number of active sites and light absorption,[32,33] because the insulator is an effective protective layer.[18,20,21,30,34,35] Consequently, MIS structures have attracted significant interest as a photoelectrode/catalyst architecture that meets the requirements of high activity and stability.[18,21,28,29,36–40] We note that the same issues can also be addressed using a thick ($\gtrsim$50 nm) insulating layer with a large number of defect states in the bulk, making the insulator electronically conductive.[41] MIS structures that have thick insulating layers tend to have higher stabilities than those with ultrathin insulators;[42] however, ultrathin insulators enable controlled tuning of their

photovoltage, which is important for reactions with multiple potential-dependent products (i.e., CO_2 and N_2 reduction).[43]

Schematics of an MIS photocathode and photoanode are presented in **Figure 1A** and **B**, respectively. The semiconductor absorbs photons and generates high-energy carriers, the insulator serves as a protective/carrier-selective layer, and the metal serves as a catalyst that promotes the electrochemical reaction. MIS photocathodes and photoanodes differ in the type of doping, the direction of band bending, and the direction in which the carriers are transported.

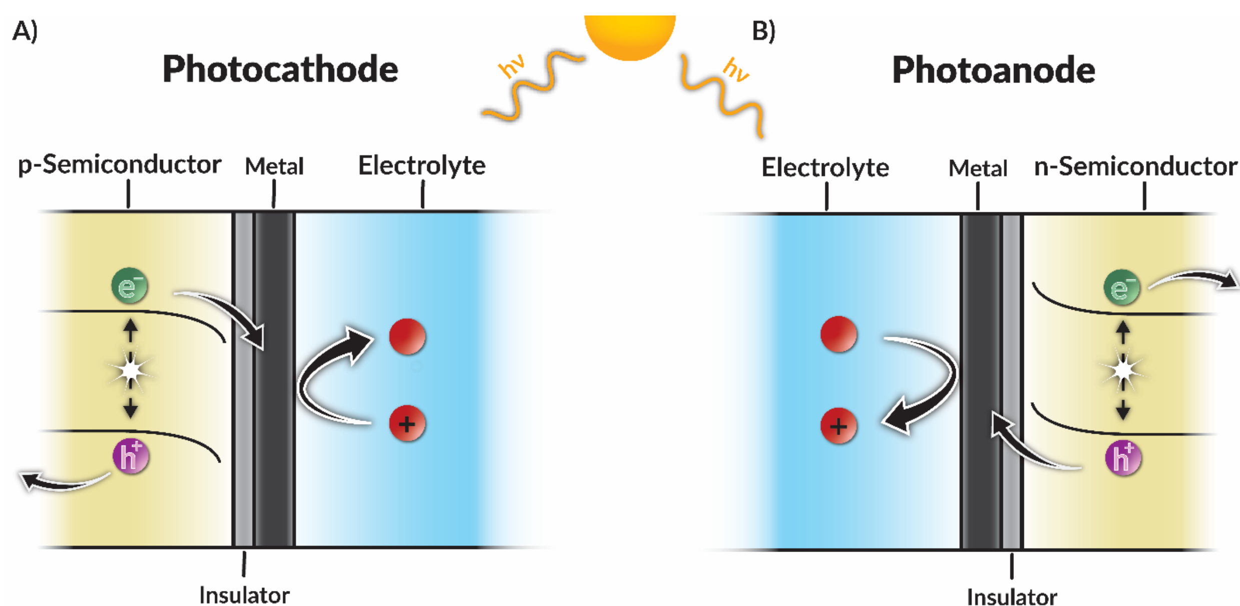

Figure 1: Illustration of the band bending, desired carrier tunneling, and reaction for a metal-insulator-semiconductor **(A)** photocathode and **(B)** photoanode.

Carriers transport from the semiconductor into the metal by quantum tunneling when the insulator thickness is $\lesssim$ 5 nm.[44] For photocathodes, the minority carrier (electrons) can readily tunnel into the metal and participate in the reduction of species adsorbed on the metal surface, while the majority carrier (holes) is collected at the dry-side of the semiconductor due to the large tunneling resistance it experiences at the semiconductor/insulator (S/I) interface. This behavior is achieved with p-type semiconductors and results in a characteristic downward bending in the

semiconductor energy bands near the S/I interface. The band bending phenomenon originates from the thermodynamic equilibrium between the semiconductor and metal, as discussed in **Section 2.1**. n-type semiconductors are used as photoanodes and experience upward band bending at the S/I interface. In photoanodes, hole (minority carrier) tunneling is facile whereas electron (majority carrier) tunneling is hindered. In practice, however, some of the majority carriers tunnel into the metal, which results in carrier recombination and reduced MIS performance. To reach performances near the theoretical maximum, a highly carrier-selective insulator is required.[21] We note that the performance of an MIS photoelectrode can be characterized by its photovoltage or its STC conversion rate because they are related; hence, the term performance will be used here to refer to both metrics.

The selectivity of an insulator is defined by its preference for minority over majority carrier tunneling, where the probability of tunneling depends exponentially on the conduction and valence band offsets (CBO and VBO, respectively).[44] The band offsets at the S/I contact form a potential barrier that carriers must tunnel through to enter the metal catalyst (see **Figure 2B)**. High recombination rates in the metal will occur if both carriers have a high tunneling probability, and low tunneling probabilities leads to small tunneling rates and, consequently, low STC rates. Thus, to promote carrier-selective tunneling, it is desired to have a high tunneling probability for the minority carrier and a low tunneling probability for the majority carrier, which could be achieved by tuning the S/I band offsets.[21,45] The effect of varying band offsets on carrier tunneling and, consequently, photovoltage and STC conversion rates has not been explored in prior MIS studies. Therefore, identifying the optimal band offset combination to achieve high performance is critical to the design of MIS photoelectrodes with high carrier selectivity.

Carrier selectivity also has a strong dependence on the insulator thickness, d, because the tunneling probability exponentially depends on it. The influence of d on the photovoltaic and photoelectrochemical performance of MIS structures is well documented in the literature.[29,30,36,46,47] Previous studies have also shown that there exists an optimum insulator thickness that provides an additional ~ 150 mV of photovoltage, relative to that obtained with just an MS structure. Modeling work by Quinn *et al.* and Card have concluded that this optimum thickness exists because the individual carrier tunneling rates are tuned by d.[36,47] Below the optimum thickness, increasing d increases the photovoltage because the majority carrier tunneling rate decreases while the minority carrier tunneling rate remains essentially constant; this has the effect of reducing electron-hole recombination in the metal. Increasing d beyond its optimum reduces the tunneling rates of both carriers and, consequently, decreases the photovoltage. Beyond the optimum d, both carriers are limited by tunneling because of the very low tunneling probabilities. However, below the optimum d, the minority carrier tunneling rate is essentially constant because its transport into the metal is limited by its diffusion to the semiconductor surface, rather than tunneling across the insulator. The majority carrier transport is limited by tunneling at all thicknesses because it has a large concentration due to the dopant; therefore, diffusion to the S/I interface is never a limitation. While this explanation describes the observed trends in photovoltage with changing insulator thickness, it does not address how the insulator thickness alters quasi-Fermi levels, which defines the photovoltage. We also note that the role of the potential drop across the insulator (resulting from interfacial charge build up) in tuning individual carrier tunneling rates and in defining the optimum insulator thickness is not known. Continuum modeling is a good tool to develop a complete understanding of how the insulator thickness alters the MIS photovoltage, as well as to optimize the S/I band offsets and guide the discovery of carrier-selective

insulating materials, a current challenge to further improving MIS performance.[21] Additionally, for systems that experience potential-dependent product selectivity (*e.g.*, CO_2 and N_2 reduction), knowledge of how insulator properties impact the photovoltage is vitally important for ensuring MIS operation at the potential that maximizes formation of a desired product.[43]

In this study, we present a comprehensive model for MIS photoelectrodes that accounts for photo-absorption and carrier generation/recombination, carrier and electrolyte transport, and interfacial tunneling and kinetics. This model improves upon previous efforts by accounting for nonidealities at the MIS interface and for transport in the electrolyte. The model is validated against experimentally measured polarization curves and photovoltage as a function of insulator thickness for a Pt/HfO_2/p-Si MIS structure, for which Linic and coworkers have presented experimental data.[23] This MIS system uses a bilayer metal structure (Pt/Ti), rather than just Pt, in order to create a high MS barrier and theoretical maximum photovoltage, as discussed in more detail later. The model is then used to understand how the insulator thickness as well as the CBO and VBO impact MIS performance and provide recommendations for obtaining high-performing MIS photoelectrodes.

2. Theory and Computational Methods

This section outlines the theory and assumptions underlying the model of MIS photoelectrodes. While the model is developed for PEC H_2 evolution (PEC HER), it can be employed for other PEC reactions (*e.g.*, CO_2 or N_2 reduction or H_2O oxidation). Our objective is to give the reader the background necessary to interpret the simulation results, as well as a framework for modeling MIS photoelectrode systems. A discussion of how the simulation results for this HER photocathode relate to a photoanode is provided in **Section S1**.

A diagram of the MIS photoelectrode modeling domain is presented in **Figure 2A**. The one-dimensional MIS model contains a semiconductor domain, an ultrathin ($\lesssim$ 3 nm) insulator layer, a thin (5−20 nm) catalyst layer, an electrolyte mass-transport boundary layer, and bulk electrolyte. Within the semiconductor domain, the drift-diffusion and Poisson equations are used to model charge-carrier transport.[44] Electrolyte transport in the boundary layer is determined using the Nernst-Planck equation and the electroneutrality constraint, which neglects the electrolyte double layer because its influence is only transient and our simulation is at steady state.[48] The MIS interface is treated as a coupled boundary condition at which the generated photovoltage drives the electrochemical reaction and the tunneling current density matches the rate of the surface reaction. The tunneling current is determined by MIS tunnel diode theory,[49] whereas the rate of reaction at the catalyst surface is represented by a Tafel equation.[48] This modeling framework captures all relevant phenomena for an MIS photoelectrode/catalyst.

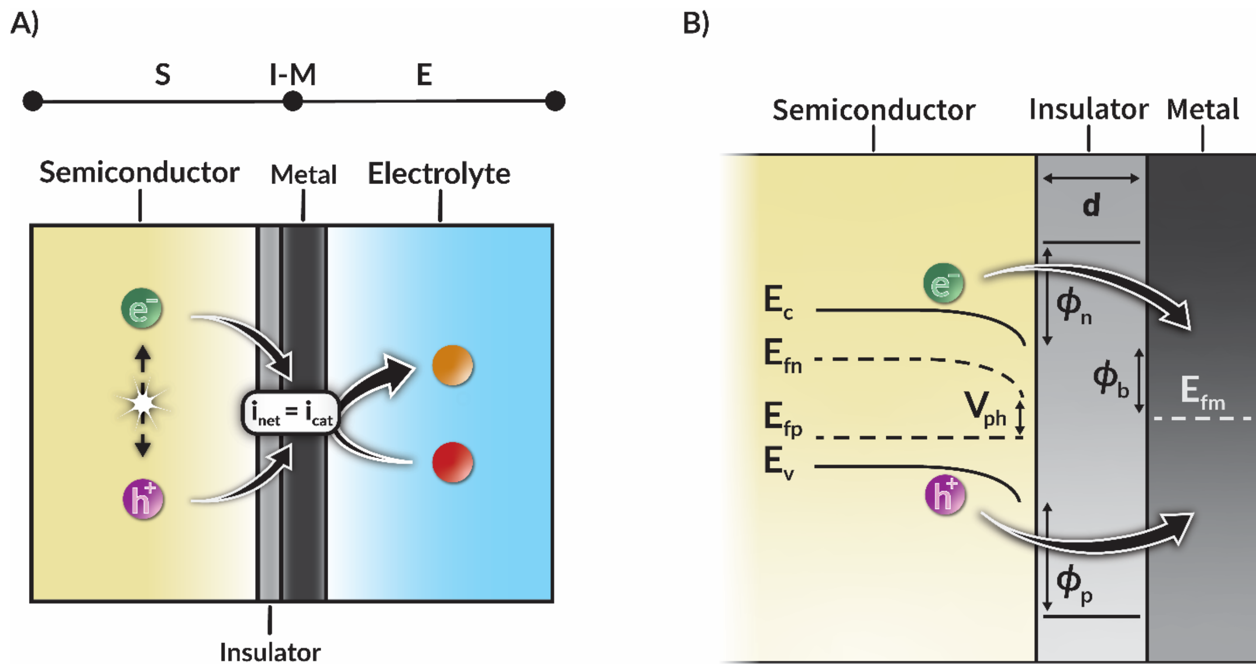

Figure 2: Schematic representation of the **(A)** one-dimensional MIS photoelectrode model and **(B)** p-type metal-insulator-semiconductor interface.

Figure 2B illustrates a simplified band energy diagram for an MIS photocathode structure involving a p-type semiconductor. Here, E_c and E_v are the conduction and valence band energy, respectively, E_{fn} and E_{fp} are the quasi-Fermi level of electrons and holes, respectively, E_{fm} is the Fermi level of the metal (also called the metal work function when referenced to vacuum), and V_{ph} is the generated photovoltage. Additionally, d is the insulator thickness, ϕ_b is the Schottky barrier, and ϕ_n and ϕ_p are the electron and hole tunneling barrier, respectively. Upon illumination of the semiconductor, the single Fermi level splits into an electron quasi-Fermi level and a hole quasi-Fermi level because the minority carrier concentration well exceeds its intrinsic concentration (see eqn. 15 below), whereas the majority carrier remains near its intrinsic concentration because the majority carriers generated by illumination is negligible compared to that introduced by doping.[44] The difference in the quasi-Fermi levels at the S/I interface is the ideal photovoltage generated by the semiconductor,[21,44] and is related to the driving force for the electrochemical reaction occurring on the catalyst surface. The current generated by the electrochemical reaction must match the net tunneling current from the semiconductor into the metal because this system is series connected without any accumulation or charging/discharging effects in the electrolyte. The net tunneling current is the sum of electron and hole currents, which is the difference in the rate of carrier transport from the semiconductor into the metal and from the metal into the semiconductor. This tunneling current is hindered by the aforementioned barrier heights. The Schottky barrier is defined as the difference between the semiconductor conduction band energy at the surface and the Fermi level of the metal, and affects the rate of carrier emission from the metal into the semiconductor.[21,37,44,47] The electron and hole tunneling barrier heights are simply the CBO and VBO of the semiconductor and insulator, respectively.[21,47,49,50] It is noted that these barrier heights

are idealized; **Section 2.5** discusses the required modifications to these idealized barrier heights to account for nonidealities at the S/I interface.

2.1. Thermodynamic Equilibrium at the Metal-Semiconductor Interface

Because both majority and minority carriers tunnel through the insulator, the thermodynamic equilibrium for an MIS structure is identical to that for a metal/semiconductor (MS) interface. The discussion of an MS contact is developed in the absence of interfacial nonidealities. **Figure 3A** illustrates the band diagram for a low work-function metal and a p-type semiconductor. χ and ϕ_m are the electron affinity and metal work function, respectively. In this case, the semiconductor and metal are not at equilibrium and, hence, their Fermi levels are not equal. The difference between the metal and semiconductor Fermi levels is the flat-band potential (also known as the built-in potential), V_{fb}, which is the maximum photovoltage for a MIS structure.[21] If the semiconductor and metal are allowed to communicate (*i.e.*, through carrier tunneling) their Fermi levels equilibrate because charge-carriers flow from the semiconductor to the metal (**Figure 3B**).[44] The resulting change in carrier concentrations alters the electric field, as determined by the Poisson equation, and causes the bands to bend.

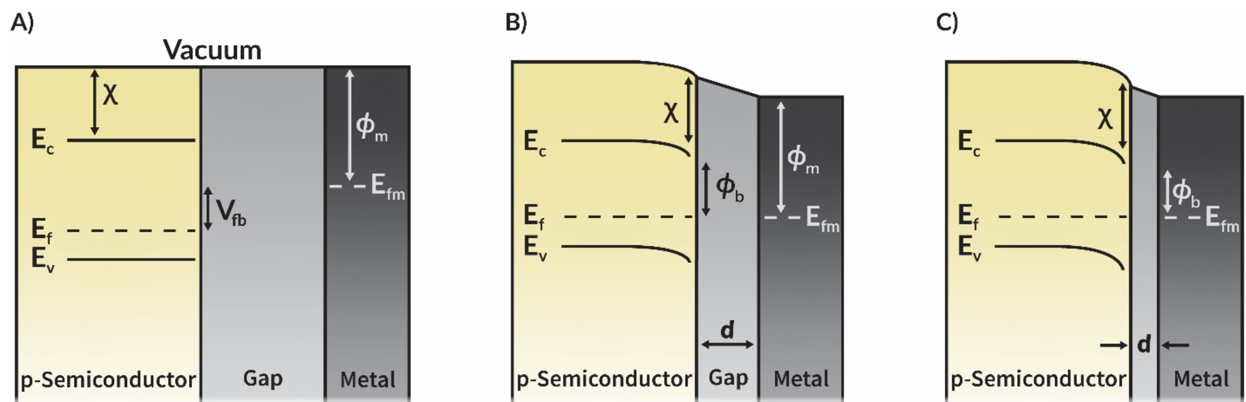

Figure 3: Energy band diagrams of an MIS photocathode at a **(A)** large gap distance, **(B)** moderate gap distance with low carrier tunneling, and **(C)** low gap distance with considerable tunneling.

As the metal and p-type semiconductor are brought close together, the tunneling of holes increases, which causes a buildup of positive charge at the metal surface. For charge neutrality to hold, an equal and opposite charge (negative) must exist at the semiconductor surface. The buildup of negative charges near the semiconductor surface causes the bands to bend downward by increasing the magnitude of the electric field at the interface. The semiconductor bands no longer bend when the applied potential, or generated photovoltage, is at V_{fb}, which is the maximum attainable photovoltage. A small gap, as shown in **Figure 3C**, reflects exactly what is seen in MIS systems. This thermodynamic analysis for an MIS photoanode is given in **Figure S1**. We note that the explanation given above remains unchanged when the MIS photoelectrode is placed in an electrolyte. Experimental evidence has shown the Fermi level of the electrolyte solution is completely screened out by the metal layer,[33] indicating that the semiconductor and metal will equilibrate without any influence from the electrolyte.

2.2. Semiconductor Physics

Charge-carrier transport within the bulk of the semiconductor is governed by the steady-state carrier continuity expressions:

$$(\boldsymbol{\nabla} \cdot \boldsymbol{N_n}) = U \tag{1}$$

$$\left(\boldsymbol{\nabla} \cdot \boldsymbol{N_p}\right) = -U \tag{2}$$

where $\boldsymbol{N_n}$, $\boldsymbol{N_p}$, are the electron and hole fluxes, respectively, and U is the net carrier generation/recombination rate. The flux of the charge-carriers is specified by the drift-diffusion equations,

$$\boldsymbol{N_n} = -nu_n\boldsymbol{\nabla}V + D_n\boldsymbol{\nabla}n \tag{3}$$

$$\boldsymbol{N_p} = -pu_p\boldsymbol{\nabla}V - D_p\boldsymbol{\nabla}p \tag{4}$$

where n, p, u_n, u_p, D_n, and D_p are the electron concentration, hole concentration, electron mobility, hole mobility, electron diffusion coefficient, and hole diffusion coefficient, respectively. In eqn. 4, V is the electric potential, which is calculated by the Poisson equation,

$$\boldsymbol{\nabla} \cdot (-\varepsilon_s \boldsymbol{\nabla} V) = q(p - n + N_d^+ - N_a^-), \tag{5}$$

where ε_s, q, N_d^+, and N_a^- are the permittivity of the semiconductor, fundamental charge of an electron, donor doping density, and acceptor doping density. In this study, we consider a p-type semiconductor, so the donor doping density is set to zero.[44]

The net rate of carrier generation/recombination, U, is the sum of the Shockley-Reed-Hall (R_{SRH}), Auger (R_{Auger}) and direct radiative recombination (R_{rad}) mechanisms minus the position-dependent rate of carrier generation $G(x)$,[44,51]

$$U = R_{SRH} + R_{Auger} + R_{rad} - G(x) \tag{6}$$

where

$$R_{SRH} = \frac{np - n_i^2}{\tau_p(n + n_i) + \tau_n(p + n_i)}, \tag{7}$$

$$R_{Auger} = (C_n n - C_p p)(np - n_i^2), \tag{8}$$

$$R_{rad} = C_{rad}(np - n_i^2). \tag{9}$$

τ_n, τ_p, C_n, C_p, and C_{rad} are the electron lifetime, hole lifetime, electron recombination rate constant, hole recombination rate constant, and carrier recombination rate constant, respectively. The variable n_i is the intrinsic carrier concentration, defined as

$$n_i = \sqrt{N_c N_v} \exp\left(-\frac{qE_g^s}{2k_B T}\right). \tag{10}$$

G(x) is calculated by integrating over the AM 1.5G solar spectrum (simulated by NREL), considering illumination from the electrolyte side and accounting for light reflection,

$$G(x) = \int_0^{\frac{hc}{qE_g^s}} \big(1 - R(\lambda)\big)\alpha(\lambda)N(\lambda)\, exp(-\alpha(\lambda)x)\, d\lambda \tag{11}$$

where h, c, E_g^s, λ, $R(\lambda)$, $\alpha(\lambda)$, and $N(\lambda)$ are Planck's constant, speed of light, semiconductor band gap, light wavelength, reflectivity, absorption coefficient, and incident photon flux, respectively. The semiconductor will absorb photons with energy less than or equal to the semiconductor bandgap, hence the limits on the integral are from zero to the wavelength corresponding to the bandgap energy. The incident photon flux can be related to the solar irradiance by dividing by the energy of a photon,

$$N(\lambda) = \frac{I(\lambda)}{hc}. \tag{12}$$

$\alpha(\lambda)$ is taken to be that of intrinsic Si,[52] and $R(\lambda)$ is calculated using the wafer ray tracer tool by PV Lighthouse[53] for a [back contact] Cu (100 nm)|Si (300 µm)|SiO_2 (0.5 nm)|HfO_2 (1.5 nm)|Ti (5 nm)|Ni (5 nm) [catalyst] system. We assume Ni and Pt to have the same optical properties, since they have similar reflectances.[54]

Solving the coupled differential equations (eqns. 1−5) above enables calculation of the band bending near the S/I interface. The conduction and valence band energy are determined by

$$E_c = -(\chi_s + V), \tag{13}$$

$$E_v = -(\chi_s + E_g^s + V). \quad (14)$$

The quasi-Fermi level levels can be determined through the Boltzmann relation:

$$E_{fn} = E_c + \frac{\mathrm{k_B T}}{\mathrm{q}} \ln\left(\frac{n}{N_c}\right) \quad (15)$$

$$E_{fp} = E_v - \frac{\mathrm{k_B T}}{\mathrm{q}} \ln\left(\frac{p}{N_v}\right) \quad (16)$$

where $\mathrm{k_B}$, N_c, and N_v are the Boltzmann constant and the effective density of states of electrons and holes, respectively. The Boltzmann relation neglects nonidealities occurring at high carrier concentrations; these effects should be included in future improvements of the model.[48]

It is important to note that the quasi-Fermi level levels depend on both the charge-carrier concentrations and the electric potential, whereas the conduction and valence band depend only on the electric potential. This dependence on carrier concentration causes a difference in how the quasi-Fermi levels bend near the S/I interface, which ultimately impacts the photovoltage (V_{ph}). V_{ph} is defined as the difference in quasi-fermi levels at the semiconductor surface added by the potential drop across the insulator (Δ),

$$V_{ph} = (E_{fn}^{ss} - E_{fp}^{ss}) + \Delta. \quad (17)$$

Δ is added to the difference in quasi-Fermi levels because it is negative and defined as the potential at the metal-insulator interface minus that at the semiconductor-insulator interface. Thus, this definition determines the photovoltage applied to the metal catalyst. The calculation for Δ is outlined in **Section 2.5**.

2.3. Electrochemical Transport and Homogeneous Reactions

Steady-state species conservation governs the transport of species within the mass-transport boundary layer of the electrolyte,

$$\boldsymbol{\nabla} \cdot \boldsymbol{N}_i = R_i. \tag{18}$$

Here, $\boldsymbol{N}_i$ is the flux of species *i,* and R_i is the volumetric rate at which species *i* is generated due to homogeneous buffer reactions. In this study, we modeled the fluxes of OH^-, H^+, and ClO_4^-. The Nernst-Planck equation is used to calculate the molar flux of species i,[48]

$$\boldsymbol{N}_i = -D_i \, \boldsymbol{\nabla} c_i - \frac{z_i \mathrm{F}}{RT} D_i c_i \boldsymbol{\nabla} V_l, \tag{19}$$

where D_i, c_i, z_i are the diffusivity, concentration, and charge of species i, respectively, V_l is the liquid-phase potential of the electrolyte, F is Faraday's constant, *R* is the ideal-gas constant, and *T* is the temperature. The first term in eqn. 19 describes the transport of species by diffusion, and the second term describes charged species migration.[48] Although the model can deviate from the dilute-solution conditions necessary for the Nernst-Planck equation to hold rigorously, the simulated current densities do not exceed 35 mA cm^{-2}, for which dilute-solution theory has been found to be sufficiently accurate.[55] Electroneutrality,

$$\textstyle\sum_i \; z_i c_i = 0, \tag{20}$$

is assumed and provides a constraint to calculate the liquid-phase potential.

The homogeneous bulk reactions considered in this model, captured by the source term, $R_{B,i}$, are

$$\mathrm{H_2O} \overset{k_w, k_{-w}}{\leftrightarrow} \mathrm{H^+ + OH^-} \qquad K_w \tag{21}$$

$$\mathrm{HClO_4} \overset{k_1, k_{-1}}{\leftrightarrow} \mathrm{H^+ + ClO_4^-} \qquad K_1 \qquad (22)$$

where $k_{n/-n}$ and K_n are the rate coefficients and the equilibrium constant for reaction n, respectively. Because of the large equilibrium constant for $HClO_4$ dissociation, we neglected this buffer reaction and assumed that $HClO_4$ was completely dissociated. k_{-n} is calculated from the relationship

$$\mathrm{k_{-n}} = \frac{k_n}{K_n}, \qquad (23)$$

and $R_{B,i}$ is given by[56]

$$R_i = \sum_n s_{i,n} \left(k_n \prod_{s_{i,n}<0} c_i^{-s_{i,n}} - \frac{k_n}{K_n} \prod_{s_{i,n}>0} c_i^{s_{i,n}} \right), \qquad (24)$$

where $s_{i,n}$ is the stoichiometric coefficient for species i in reaction n, and a_i is the activity of species i.

2.4. Reaction Kinetics

The following electrochemical reaction occurs at the Pt surface.

$$2\mathrm{H^+} + 2\mathrm{e^-} \rightarrow \mathrm{H_2}, \quad U_{HER}^{o} = 0\ \mathrm{V\ vs.\ SHE} \qquad (25)$$

Because of the highly acidic electrolyte environment considered (1 M $HClO_4$), we neglect the HER reaction process for alkaline conditions. The HER current density was determined through the concentration-dependent Tafel expression,

$$i_{HER} = -i_o^{HER} \left(\frac{c_{H^+}}{c_{ref}} \right)^{1-\frac{\alpha_{HER}}{n}} \exp\left(-\frac{\alpha_{HER} F}{RT} \eta \right), \qquad (26)$$

where i_o^{HER}, n, α_{HER}, and η are the exchange current density, number of electrons transferred, transfer coefficient, and surface overpotential for HER, respectively. c_{ref} is a reference concentration defined as 1 M. If multiple reactions occur, then each reaction requires its own concentration-dependent Tafel equation, and the net electrocatalysis current (eqn. 29) would include a summation over each product current density. i_o^{HER} and α_{HER} were determined through a Tafel analysis of the data reported by Quinn *et al.* (see **Figure S2**) and are provided in **Table S1**.[23] The surface overpotential is given by

$$\eta = \mathrm{V}_{cat} - \mathrm{V}_l - \left(U_{HER}^{o} - 2.303 \frac{RT}{F} \mathrm{pH} \right), \quad (27)$$

where V_{cat} is the potential of the metal catalyst and V_l and pH are the liquid-phase potential and pH adjacent to the Pt surface, respectively. V_{cat} is defined by the negative of the electron quasi-Fermi level at the semiconductor surface plus the potential drop across the insulator.

$$\mathrm{V}_{cat} = -\left(E_{fn}^{ss} + \Delta \right) \quad (28)$$

A derivation and explanation of this definition is provided in **Section S4**, which shows that V_{cat} is consistent with summing over the applied, generated, and loss potentials (**Figure S3**).

According to the Tafel equation (eqn. 26), the HER current density will rise exponentially with catalyst potential; however, this system will eventually become limited by the photocurrent generated by the semiconductor. The current continuity constraint ensures the HER current does not exceed the photocurrent limit, but this constraint alone leads to convergence difficulties. To help reach simulation convergence, we employ a Koutecký - Levich type equation,[48]

$$i_{cat} = \frac{i_{HER}}{1 + \left| \frac{i_{HER}}{i_{lim}} \right|}, \quad (29)$$

where i_{lim} is set by the flux of the minority carrier due to drift and diffusion at the semiconductor surface. In other words, i_{lim} is reached when all the minority carriers entering the MIS interface by drift and diffusion tunnel into the metal and do not recombine.

2.5. Interfacial Carrier Transport and Nonidealities

At the semiconductor surface, charge-carriers either tunnel into the metal and/or recombine at trap sites at the S/I interface. The tunneling current density is determined using MIS tunnel diode theory developed by Card and Rhoderick:[49]

$$i_n = -k_n P_{T,n}\left(n_{ss} - n_{eq}\right) \tag{30}$$

$$i_p = k_p P_{T,p}\left(p_{ss} - p_{eq}\right) \tag{31}$$

$$i_{net} = i_n + i_p \tag{32}$$

where k_n, k_p, $P_{T,n}$, $P_{T,p}$, n_{eq}, and p_{eq} are the electron and hole tunneling rate coefficient, tunneling probability, and equilibrium concentration, respectively; the subscript ss denotes values at the semiconductor surface. Here, i_n, i_p, and i_{net} are the electron, hole, and net tunneling current density, respectively. A detailed derivation of eqns. 30–32 is given in **Section S5**. The electron and hole tunneling rate coefficients are given by

$$k_n = \frac{4m_n^s \pi q (k_B T)^2}{h^3 N_c}, \tag{33}$$

$$k_p = \frac{4m_p^s \pi q (k_B T)^2}{h^3 N_v}. \tag{34}$$

The tunneling probabilities are determined by assuming a rectangular potential tunneling barrier.

$$P_{T,n} = \exp\left(-\alpha_n d \sqrt{\phi_n}\right) \tag{35}$$

$$P_{T,p} = \exp\left(-\alpha_p d \sqrt{\phi_p}\right), \tag{36}$$

where α_n, α_p, and d are the electron and hole tunneling coefficients, respectively, and the insulator thickness. The tunneling coefficients are given by

$$\alpha_n = \frac{4\pi\sqrt{2m_n^I}}{h}, \tag{37}$$

$$\alpha_p = \frac{4\pi\sqrt{2m_p^I}}{h}, \tag{38}$$

where m_n^I and m_p^I are the effective electron and hole masses of the insulator. The equilibrium carrier concentrations (n_{eq} for electrons and p_{eq} for holes) are related to the Schottky barrier by

$$n_{eq} = N_c \exp\left(-\frac{q\phi_b}{k_B T}\right) \tag{39}$$

$$p_{eq} = N_v \exp\left(-\frac{q(E_g^S - \phi_b)}{k_B T}\right). \tag{40}$$

The recombination current density due to interfacial trap sites ($i_{n,R}$ for electrons and $i_{p,R}$ for holes) is approximated by discrete energy levels and are assumed to be donor type, which are commonly seen in systems with oxide films deposited on Si by chemical vapor deposition,[57]

$$i_{n,R} = q\theta_n v_{th} N_t (n - nf_t - \frac{n_i}{g_D} f_t) \tag{41}$$

$$i_{p,R} = q\theta_p v_{th} N_t (pf_t + g_D(n_i f_t - n_i)), \tag{42}$$

where θ_n, θ_p, v_{th}, N_t, f_t, and g_D are the average electron and hole capture cross-section, respectively, thermal velocity, total number of interfacial trap sites, trap site occupation fraction,

and the degeneracy factor (assumed to be one). N_t is calculated using experimentally measured trap densities (D_{it}), which changes with insulator thickness,

$$N_t = \frac{D_{it}(d)\left(\psi + V_p - \phi_0\right)}{f_t}, \tag{43}$$

where ψ is the band bending potential, V_p is the difference in quasi-fermi level of holes and the valence band energy, and ϕ_0 is the neutral energy level (depicted in **Figure 4**). Above ϕ_0 the trap states are acceptor type (neutral when empty and negatively charged when full), and below ϕ_0 they are donor type (positively charged when empty and neutral when full of electrons). The trap-site occupation fraction is determined by enforcing the following steady-state constraint:

$$i_{n,R} = i_{p,R} \tag{44}$$

The thickness dependence of D_{it} is approximated by taking a linear fit of experimental data for Si/SiO_2, shown in **Figure S4**.[49] These interface trap sites have been shown to have a weak Fermi level pinning effect (where the semiconductor Fermi level is pinned to the energy of the defect rather than the metal Fermi level),[58] which is assumed to be negligible in the current model. We also neglect any metal-induced gap states (MIGS) within the semiconductor bandgap that would pin the semiconductor Fermi level to the charge neutrality level of the MIGS, since the insulator is known to mitigate Fermi level pinning by attenuating the metal electron wavefunction.[25,26] However, at low-to-moderate insulator thicknesses, a degree of Fermi-level pinning may exist,[25] and this nonideality should be accounted for in future developments of the model.

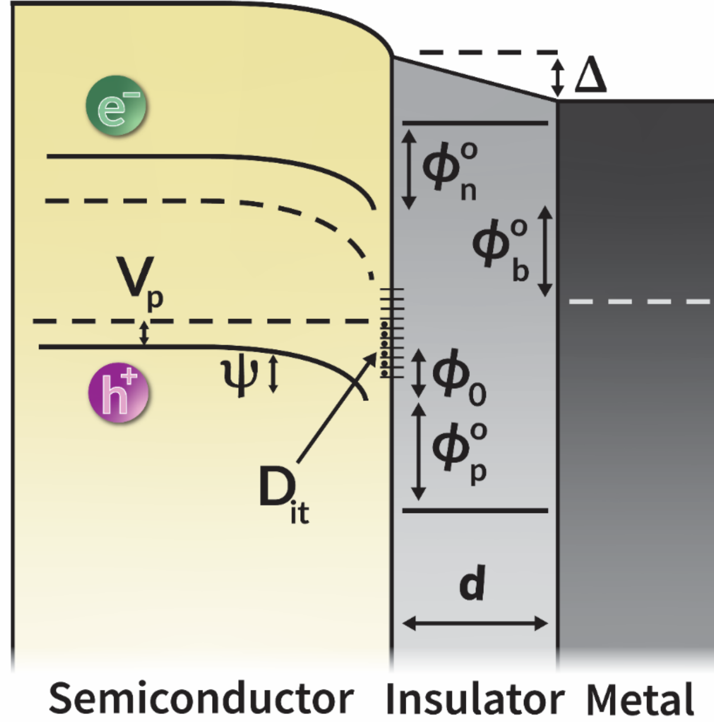

Figure 4: Energy band diagram, with nonidealities considered in the model, of a p-type semiconductor in contact with an insulator and low work function metal.

In practice, a potential drop across the insulator and an image force exists, which reduce the ideal barrier heights. This potential drop occurs because of charge build up across the interface, which results in a potential drop (Δ) that reduces the reaction driving force (**Section 2.4**) and barrier heights. Thus,

$$\Delta = -\frac{Q_m}{C}, \tag{45}$$

where Q_m is the charge on the metal and C is the interfacial capacitance. A derivation of eqn. 45 is shown in **Section S7**. Q_m can be determined from a charge balance across the MIS interface, accounting for charge at the semiconductor surface (Q_{ss}), charge at the interface trap sites (Q_{it}), and the fixed charge on the insulator (Q_{fix}),[44]

$$Q_m = -\left[Q_{ss} + Q_{it} + Q_{fix}\right] \quad (46)$$

$$Q_{ss} = -\frac{\varepsilon_s}{d_n}(V_{sI} + \Delta - V_s) \quad (47)$$

$$Q_{it} = -qD_{it}(\psi + V_p - \phi_0) \quad (48)$$

Q_{ss} is calculated by treating the semiconductor surface as a dielectric capacitor. V_{sI} is the potential at the S/I interface in the absence of potential drop and is solved iteratively until the tunneling and reaction current are equal. V_s is the potential at the semiconductor surface and d_n is the distance between the SI boundary and the closest node inside the semiconductor domain. Eqn. 48 is used to calculate the charge due to carriers trapped at the interface; the term in parenthesis is simply the energy difference between the hole quasi-Fermi level at the semiconductor surface and the neutral energy level (ϕ_0). Multiplying this quantity by the interface-trap density (D_{it}) yields the number of interface states above ϕ_0 that are filled. Eqns. 45-48 are used to solve for Δ

$$\Delta = \frac{Q_{fix} - \frac{\varepsilon_s}{d_n}(V_{sI} - V_s) - qD_{it}\left(\psi + V_p - \phi_0\right)}{C + \frac{\varepsilon_s}{d_n}}. \quad (49)$$

For MIS structures involving semiconductors with a native oxide layer on their surface (*e.g.*, Si), the native oxide will contribute to the capacitance across the insulator. To account for both the native oxide and the insulator influence on C, we use the following relationship for capacitors in series:

$$C = \frac{1}{\frac{d}{\varepsilon_I} + \frac{1}{C_{ox}}} \quad (50)$$

Here, ε_I is the insulator permittivity and C_{ox} is the capacitance of the native SiO_2 layer, which is a fitted parameter (1.5 μF cm^{-2}) because its thickness nor permittivity are well defined. The fitted value of C_{ox} is quite close to previously reported values of the native SiO_2 capacitance.[30] The charges built up at the semiconductor and metal surfaces (image-force charges) exert an electrostatic attractive force that effectively reduces the barrier heights. This phenomenon is referred to as image-force barrier lowering, and its potential ($\Delta\phi$) is given by

$$\Delta\phi = \sqrt{\frac{q|\mathbb{E}_{ss}|}{4\pi\epsilon_s}} \tag{51}$$

where

$$\mathbb{E}_s = -\frac{dV_{ss}}{dx}. \tag{52}$$

Here, $\mathbb{E}_{ss}$ is the electric field at the semiconductor surface, which is calculated by eqn. 56, and V_{ss} is the electric potential at the semiconductor surface. The modifications to the barrier heights resulting from these nonidealities are[44,50]

$$\phi_b = \phi_b^o - \Delta - \Delta\phi \tag{53}$$

$$\phi_n = (\phi_n^o - \varphi) + \frac{\Delta + \Delta\phi}{2} \tag{54}$$

$$\phi_p = (\phi_p^o - \varphi) - \frac{\Delta + \Delta\phi}{2} \tag{55}$$

Here, ϕ_b^o, ϕ_n^o, and ϕ_p^o are the idealized barrier heights, as defined at the beginning of Section 2 and in **Figure 4**. For the tunneling barrier heights, a mean approximation is used to capture the effects of nonidealities.[50] Moreover, we introduce a fitting parameter (φ) that accounts for the

differences between bulk and ultrathin film CBO and VBO.[37] Physically, φ represents the decrease in the insulator bandgap due to oxygen vacancies and the formation of a mixed metal-oxide. The baseline MIS system uses Ti as an adhesion layer between the Pt catalyst and HfO_2 as the insulator. Ti is known to react with metal-oxides at their interface to form TiO_2, which introduces oxygen vacancies in the metal-oxide insulator, significantly lowering its bandgap.[59] This process also forms a mixed HfO_2-TiO_2 insulator that has a lower bandgap than HfO_2 alone.[60] φ reduces the bandgap of HfO_2 by 2 eV, which is reasonable for the aforementioned phenomenon.

We note that alternative interfacial transport mechanisms, other than direct tunneling (*e.g.*, Fowler-Nordheim tunneling, Poole-Frenkel emission, and trap-assisted tunneling (TAT)), can also occur.[44] However, these alternative charge transport mechanisms are not expected to dominate over direct tunneling for insulator thicknesses below ~ 5 nm and at room temperature,[44] which are the conditions explored in this study. **Figure S6** presents the modeled TAT current density as a function of insulator thickness and shows that TAT is negligible except for at low thicknesses when there is a high density of bulk trap states and/or a shallow trap depth. However, at low thicknesses, the density of bulk trap states and the trap depth are expected to be low and high, respectively. As a result, the TAT mechanism is not included in the model results. Further discussion on the TAT mechanism is provided in **Section S8**. A fully comprehensive MIS model should account for alternative mechanisms, since under certain conditions they may dominate over direct tunneling. However, incorporation of multiple interfacial carrier transport mechanisms is beyond the scope of the current study but should be considered in future work.

2.6. Boundary Conditions

The boundary conditions for the model developed here are listed in **Table 1** and illustrated in **Figure 5A**. They consist of Dirichlet conditions at the edge of the boundary layer and the dry-side

of the semiconductor and Neumann boundary conditions at the interface of the semiconductor and electrolyte domains. At the edge of the boundary layer, the species concentrations are set equal to those in the bulk electrolyte at equilibrium, and the liquid-phase potential is set to zero as a reference.[56] At the metal catalyst surface, the flux of species k (N_k) is related to its current density through Faraday's law:

$$N_k = -\frac{i_k}{n_e F}. \tag{56}$$

This flux (or current density) must be equivalent to the net flux of charge-carriers tunneling from the semiconductor into the metal, as this system is effectively a set of resistors in series at steady state. The flux of electrons from into the metal is the net tunneling current density divided by the charge of an electron,

$$N_n = \frac{i_{net}}{q}. \tag{57}$$

At the dry-side of the semiconductor, an ohmic contact boundary condition is used, which assumes equilibrium between the semiconductor and metal ohmic contact. The equilibrium carrier concentrations and electric potential are

$$n_{eq}^{oc} = -\frac{1}{2}N_a^- + \frac{1}{2}\sqrt{N_a^{-2} + 4n_i^2}, \tag{58}$$

$$p_{eq}^{oc} = \frac{1}{2}N_a^- + \frac{1}{2}\sqrt{N_a^{-2} + 4n_i^2}, \tag{59}$$

$$V_{eq} = \frac{k_B T}{q}\left[\ln\left(\frac{n_{eq}^{oc}}{n_i}\right) + \frac{1}{2}\ln\left(\frac{N_v}{N_c}\right)\right] - \frac{E_g}{2} - \chi. \tag{60}$$

The derivation of eqns. 58-60 is given in **Section S9**. We note that, although equilibrium at this boundary is likely nonphysical, in practice it is often assumed and is reasonable given that this boundary is far from the area of interest (*i.e.*, the S/I interface).[61]

Table 1: List of boundary conditions.

Dependent Variable	Ohmic Contact | Semiconductor	Boundary Layer | Bulk Electrolyte	Units
$\boldsymbol{n}$	n_{eq}^{oc}	–	cm^{-3}
$\boldsymbol{p}$	p_{eq}^{oc}	–	cm^{-3}
$\boldsymbol{V}$	$V_{app} + V_{eq}$	0	V
$\boldsymbol{C_{H^+}}$	–	1.0	mol m^{-3}
$\boldsymbol{C_{OH^-}}$	–	10^{-14}	mol m^{-3}
$\boldsymbol{C_{ClO_4^-}}$	–	1.0	mol m^{-3}

2.7. Physical Parameters

The physical parameters used in this study are presented in **Table 2**. Here, the properties of the semiconductor are those for p-Si, the properties of the insulator are for HfO_2, and the properties of the catalyst are for Pt. This Pt/HfO_2/p-Si MIS structure was chosen because its performance as a function of HfO_2 thickness has been well characterized for PEC HER by Linic and coworkers,[23] allowing for direct model validation.

Table 2: List of model parameters.

Parameter	Value	Units	Ref.
Semiconductor			
$\boldsymbol{E_g^s}$	1.12	eV	44

$\boldsymbol{\chi_s}$	4.05	eV	44
$\boldsymbol{\varepsilon_s/\varepsilon_o}$	11.9	−	44
$\boldsymbol{L_s}$	300	μm	23
$\boldsymbol{m_n^s/m_o}$	0.33	−	44
$\boldsymbol{m_p^s/m_o}$	0.55	−	44
$\boldsymbol{u_n}$	1450	$cm^2\ V^{-1}\ s^{-1}$	61
$\boldsymbol{u_p}$	500	$cm^2\ V^{-1}\ s^{-1}$	61
$\boldsymbol{D_n}$	4.58×10^{-11}	$mol\ L^{-1}$	61
$\boldsymbol{D_p}$	56.281	s^{-1}	61
$\boldsymbol{N_a^-}$	10^{16}	cm^{-3}	23
$\boldsymbol{N_c}$	2.7×10^{19}	cm^{-3}	61
$\boldsymbol{N_v}$	10^{19}	cm^{-3}	61
$\boldsymbol{\tau_n}$	10	μs	61
$\boldsymbol{\tau_p}$	10	μs	61
$\boldsymbol{C_n}$	2.8×10^{-31}	$cm^6\ s^{-1}$	61
$\boldsymbol{C_p}$	9.9×10^{-32}	$cm^6\ s^{-1}$	61
$\boldsymbol{C_{rad}}$	1.1×10^{-14}	$cm^3\ s^{-1}$	61
Electrochemical			
$\boldsymbol{D_{H^+}}$	9.312×10^{-5}	$cm^2\ s^{-1}$	48
$\boldsymbol{D_{OH^-}}$	5.26×10^{-5}	$cm^2\ s^{-1}$	48
$\boldsymbol{D_{ClO_4^-}}$	1.792×10^{-5}	$cm^2\ s^{-1}$	48
$\boldsymbol{k_w}$	1.4×10^{-3}	$mol\ L^{-1}\ s^{-1}$	43

$\boldsymbol{K_w}$	10^{-14}	M^2	1
$\boldsymbol{U_{HER}^o}$	0	V vs SHE	1
$\boldsymbol{L_{bl}}$	100	µm	assumed
Interfacial			
$\boldsymbol{Q_{fix}}$	72.1	$\mu C\ cm^{-2}$	62
$\boldsymbol{\varepsilon_I/\varepsilon_o}$	19	−	62
$\boldsymbol{m_n^I/m_o}$	0.14	−	63
$\boldsymbol{m_p^I/m_o}$	0.14	−	assumed
$\boldsymbol{\phi_0}$	0	eV	assumed
$\boldsymbol{\phi_n^o}$	2.1	eV	57
$\boldsymbol{\phi_p^o}$	2.4	eV	57
$\boldsymbol{\phi_m}$	4.3	eV	44
$\boldsymbol{\theta_n}$	10^{-17}	cm^2	64
$\boldsymbol{\theta_p}$	10^{-17}	cm^2	64
$\boldsymbol{\nu_{th}}$	10^5	$m\ s^{-1}$	51
$\boldsymbol{\varphi}$	1	eV	fitted
$\boldsymbol{C_{ox}}$	1.5	$\mu F\ cm^{-2}$	fitted

2.8. Numerical Methods

The governing equations (species balances, electroneutrality, and Poisson's equation) used within the Tertiary Current Distribution and Semiconductor Modules are solved with the MUMPS general solver in COMSOL Multiphysics 6.0 with a relative tolerance of 0.0001. The modeling domain was discretized with a nonuniform mesh with refinement near the S/I and metal-electrolyte

interfaces and comprised of 791 elements. A sensitivity analysis on the mesh size was performed, and the results were found to be independent for meshes greater than the 150 elements. Details on how to achieve model convergence is given in **Section S10**.

3. Results and Discussion

3.1. Model Validation

To validate the MIS photocathode model, we simulated the HER performance of the Pt/HfO_2/p-Si MIS structure investigated by Quinn *et al,*[23] as shown in **Figure 5A.** The HfO_2 layer was deposited via atomic layer deposition (ALD) using tetrakis(dimethylamino)hafnium (TDMAH) as the precursor and the insulator thickness number was determined by the number of ALD cycles.[23] The HfO_2 deposit is amorphous within the range of thicknesses reported in this study and has a stoichiometry of 2 O atoms for every Hf atom.[62] The electrolyte is contained in a beaker that has a hole on one side to which the MIS photocathode is attached. A biasing potential was applied between a metal contact on the back (dry) side of the MIS and the Pt anode; the potential between the dry side of the MIS and the electrolyte was measured using a reference electrode. **Figure 5B** illustrates all of the components of the MIS included in the simulation. In addition to p-Si, HfO_2, and Pt, we included a thin layer of Ti between the HfO_2 and Pt layers and a native SiO_2 layer between p-Si and the HfO_2 layer, since both of these elements were present in the MIS structure used by Quinn *et al*.[23] The Ti layer in contact with the Pt was used to create a higher Schottky barrier and flat-band potential than could be achieved with Pt alone, since Ti has a lower work function than Pt.[23,44] Despite their efforts to remove it, Quinn *et al.* noted that a thin layer of SiO_2 remained on the surface of p-Si.[23,36] Finally, a minimum HfO_2 thickness of 0.5 nm was used since that is its crystal lattice length;[65] hence, simulations for lower thicknesses were considered to be unphysical.

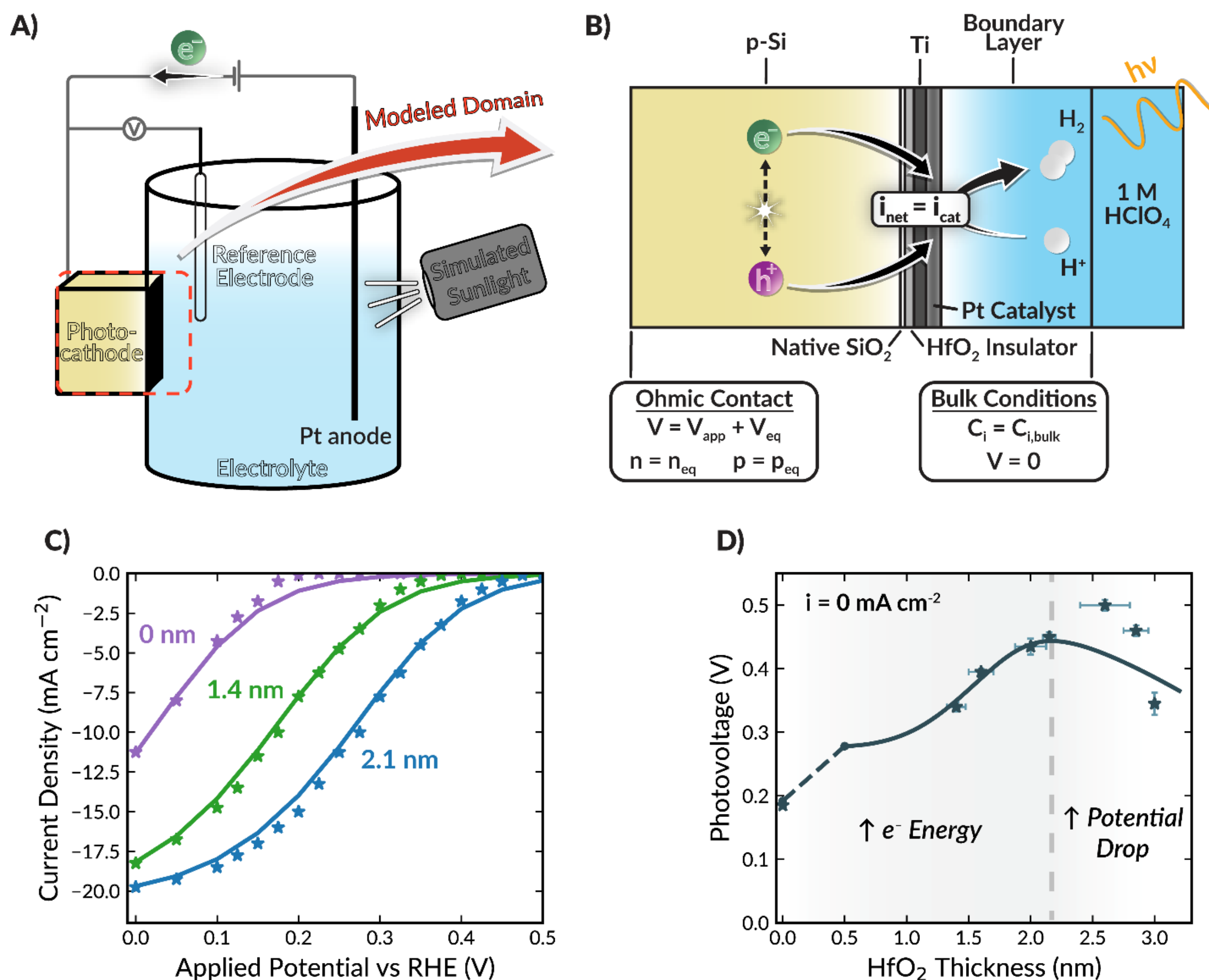

Figure 5: Diagram of the **(A)** experimental cell and **(B)** model system with its boundary conditions. Simulated (solid lines) and measured (stars) **(C)** polarization curves at varying HfO_2 thicknesses and **(D)** photovoltage as a function of HfO_2 thickness for a Pt/HfO_2/p-Si photocathode.

Figures 5C illustrates the effects of HfO_2 thickness on the polarization curve for a Pt/HfO_2/p-Si photocathode/catalyst. Good agreement with the experimental data of Quinn *et al.*[23] is achieved by adjustment of the two fitting parameters, φ and C_{ox}, listed in **Table 2**. At the equilibrium HER potential (0 V vs RHE), the system can generate hydrogen, but the rate of hydrogen generation depends on the thickness of HfO_2. Applying a positive potential reduces the current density because of the lower reaction overpotential (*i.e.*, the reaction is kinetically limited). The potential at which no current flows (*i.e.*, the onset potential) changes with HfO_2 thicknesses because of its

influence on the photovoltage. The iR-corrected photovoltage can be approximated from the experimental data by taking the difference of the onset potential between a Pt/HfO_2/p-Si photocathode/catalyst and a Pt wire.

A plot of the photovoltage at zero current density as a function of HfO_2 thickness is shown in **Figure 5D**. Here again, there is generally good agreement with the predictions of the model and the experimental data. We note that previous modeling efforts have had difficulty replicating the photovoltage dependence on insulator thickness and predicting the optimum thickness.[23,36,37] As discussed in the following section, our simulations reveal that the increase in photovoltage with HfO_2 thickness is a consequence of the increase in the energy of electrons that tunnel into the metal (*i.e.*, quasi-Fermi level of electrons at the semiconductor surface). Beyond the optimum thickness, the photovoltage decreases because of the increasing potential drop across the insulator.

Although good agreement between the model and experimental data is achieved for HfO_2 thicknesses below ~ 2 nm, some discrepancy occurs at higher thicknesses. This discrepancy is attributed to two factors: the density of interface trap sites and the capacitance of the native SiO_2 layer. The interface trap density is an experimentally measured quantity that changes with insulator thickness.[29,49] It has been reported for thicknesses $\lesssim$ 2 nm, but not for thicker insulating layers. The model extrapolates interface trap densities linearly for thicknesses > 2.2 nm (**Figure S4**), which likely leads to inaccuracies in the potential drop across the insulator. We also assume a constant capacitance for the native SiO_2 layer. This assumption is unlikely to reflect the experimental reality where each photovoltage data point is for a different MIS photoelectrode. Slight differences in the fabrication process between samples could lead to varying SiO_2 thicknesses, which, in turn, would impact the native oxide capacitance and, consequently, the interfacial potential drop. The effect of these variables on photovoltage is shown to be significant

in **Figure S7**. Despite this inaccuracy, the model adequately captures the optimum insulator thickness and the drop in photovoltage with thicker HfO_2 layers.

3.2. Photovoltage Trends with Insulator Thickness

Since the insulator thickness strongly affects the photovoltage of an MIS structure, it is desirable to understand the origins of this effect. Previous explanations for the trends in photovoltage with insulator thickness have argued that the increase is due to an increase majority carrier tunneling resistance (*i.e.*, lower tunneling rate of undesired charge) and that the decrease at larger thicknesses is a result of high tunneling resistances (*i.e.*, hindered tunneling rates) for both carriers.[21,23,47] However, this interpretation does not account for the positions of the electron and hole quasi-Fermi levels, which define the photovoltage, as well as the potential drop across the insulator.

The dependence of the photovoltage and its two components (the ideal photovoltage and insulator potential drop) on HfO_2 thickness are shown in **Figure 6A**. The ideal photovoltage greatly exceeds the measured photovoltage and increases with HfO_2 thickness up to ~ 2.5 nm, beyond which a slight decrease occurs. As seen in **Figure 6B**, the changes in the ideal photovoltage with insulator thickness is due to changes in the electron quasi-Fermi level at the semiconductor surface, as detailed in **Section 3.3**. The surface hole quasi-Fermi level is essentially constant with HfO_2 thickness for a p-type doped semiconductor because changes in the hole concentration and the electric potential with HfO_2 thickness have a negligible effect on the Fermi level compared to that due to the high dopant concentration.

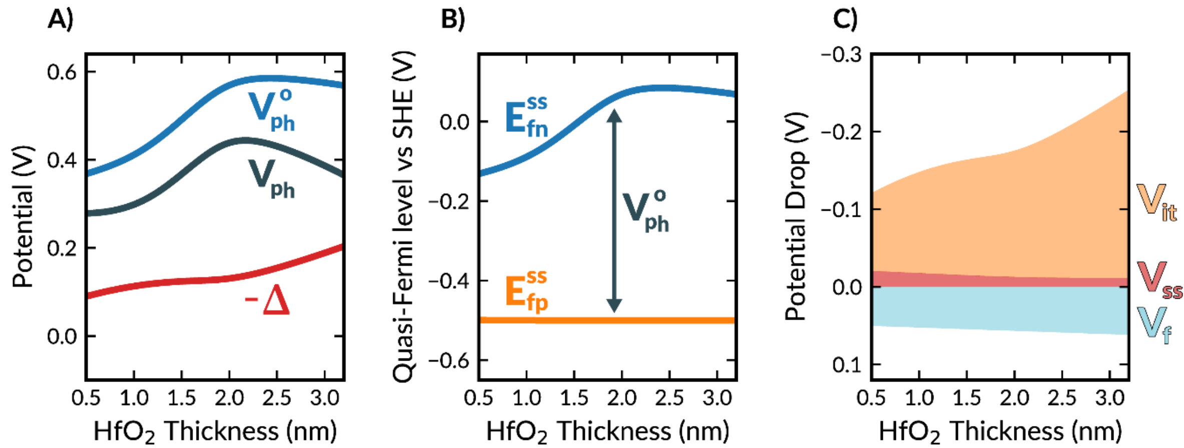

Figure 6: **(A)** Photovoltage (V_{ph}), ideal photovoltage (V^{o}_{ph}), and interfacial potential losses (Δ), **(B)** quasi-Fermi level of electrons (E^{ss}_{fn}) and holes (E^{ss}_{fp}) at the semiconductor surface, and **(C)** breakdown of interfacial potential losses as a function of insulator thickness at 0 mA cm^{-2}. V_{it}, V_{ss}, and V_{f} is the potential drop due to interfacial trap charges, accumulated charge at the semiconductor surface, and fixed insulator charge, respectively.

HfO_2 thickness influences not only the minority carrier quasi-Fermi level but also the potential drop across the insulator. **Figure 6A** shows that at ~2 nm the insulator potential drop becomes large enough to cause the photovoltage to decrease for higher HfO_2 thicknesses. While the high electron tunneling resistance causes the photovoltage to decrease slightly at high HfO_2 thicknesses (discussed in **Section S18**), the model shows this is not the primary mechanism for the decrease in photovoltage; instead, the decrease is due to the large potential drop across the insulator. **Figure 6C** shows that the main contributor to this drop is from charge trapped at the S/I interface (V_{it}), resulting from the high density of interfacial trap sites for thick insulating layers, as seen in **Figure S4**. The interfacial trap site density has been shown to increases with insulator thickness, but the origin of this trend is still unknown.[29,49] An effective method for reducing the interfacial trap density and improving the measured photovoltage is thermal annealing.[29] Compared to the interfacial trap states, the influence of the charge at the semiconductor surface (V_{ss}) and the fixed insulator charge (V_{f}) on the insulator potential drop are minor, but fixed

insulator charge could be used to reduce the drop, as discussed in **Section S12**. The results presented here are expected to be similar for a photoanode, except that the insulator thickness will lower the hole quasi-Fermi level; see **Section S1** for details.

3.3. Electron Quasi-Fermi Level Bending

As mentioned previously, the increase in photovoltage with insulator thickness is due to an increase in the electron quasi-Fermi level near the S/I interface. Understanding how this electron energy is impacted by the insulator is important for achieving further performance improvements. The influence of insulator thickness on the electron quasi-Fermi level profile is presented in **Figure 7A**, and the entire band diagram is shown in **Figure S8**. In the absence of a HfO_2 layer, the electron quasi-Fermi level drops significantly near the S/I interface, resulting in low photovoltages. Introduction of the HfO_2 layer causes less bending of the electron quasi-Fermi level near the semiconductor surface and ultimately it becomes nearly flat for thicker HfO_2 layers. Thus, by increasing the insulator thickness, the MIS structure operates closer to its flat-band potential, the maximum attainable photovoltage. The insulator thickness does this by altering the hole concentration and, consequently, the electric field at the semiconductor surface.

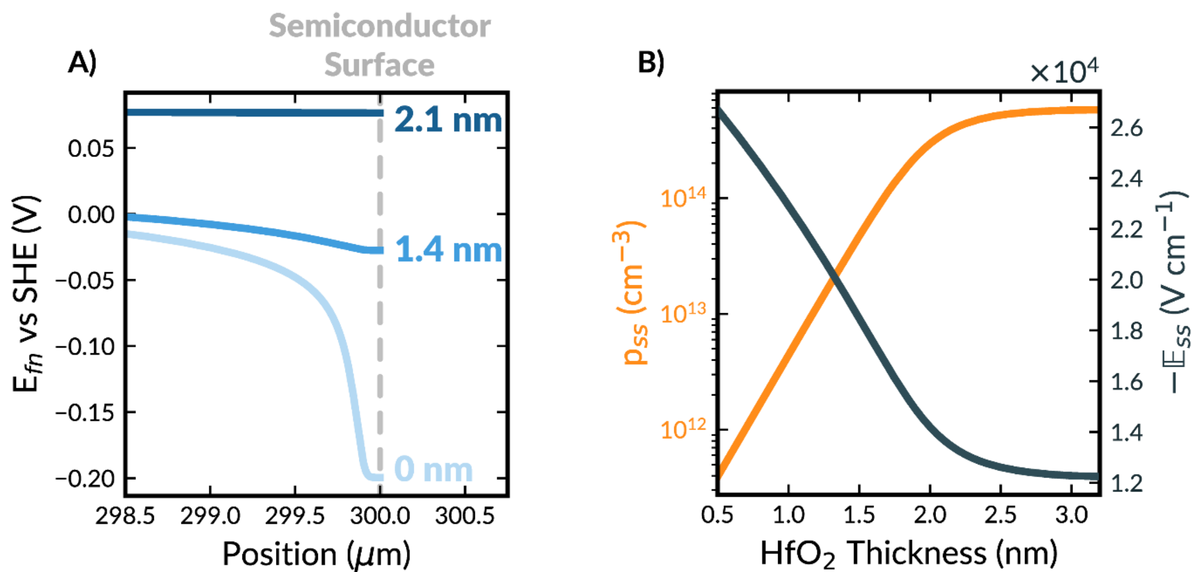

Figure 7: Profiles near the S/I interface at various HfO_2 thicknesses of the **(A)** electron quasi-Fermi level (E_{fn}). **(B)** Hole concentration (p_{ss}) and electric field ($\mathbb{E}_{ss}$) at the semiconductor surface as a function of insulator thickness. All plots are shown at 0 mA cm^{-2}.

Figure 7B shows that holes buildup at the semiconductor surface with increasing the insulator thickness, which is due to increases in the resistance to tunneling. The increased hole concentration at the semiconductor surface reduces the magnitude of the electric field, resulting in the flattening out of the electron quasi-Fermi level with HfO_2 thickness. The electric field and quasi-Fermi level of electrons are related through the Boltzmann relation (eqn. 15), since the electric field is simply the spatial derivative of the electric potential.[44] Thus, increasing the HfO_2 thickness reduces electron quasi-Fermi level bending near the semiconductor surface by increasing the hole concentration, which lowers the magnitude of the electric field at the S/I interface. This occurs until ~2.3 nm, beyond which surface recombination rate becomes larger than tunneling, see **Figures S9** and **S10**, due to the high density of interfacial trap sites.

The results provided here offer critical insight into how changing insulator thickness alters band bending and enables the MIS structure to operate closer to its flat-band potential. The extent of band bending is altered by the HfO_2 thickness because of its effects on the carrier concentrations at the semiconductor surface (see **Figure S11** for influence of HfO_2 on electron concentration). These carrier concentration effects can be further leveraged to enhance MIS performance by tuning the VBO and CBO between the insulator and semiconductor. The following sections outline the effects of tuning the band offsets and identifies prospective insulating materials that exhibit desirable band offsets with Si.

3.4. Effects of Valence- and Conduction-Band Offsets

The VBO and CBO are important properties that affect the selectivity of carrier tunneling. Both band offsets can be varied by the choice of insulating material and its doping, as has been

demonstrated for TiO_2.[66] MIS structures that exhibit high majority carrier and low minority carrier band offsets between the insulator and semiconductor (asymmetric band offsets) are commonly thought to achieve highly selective carrier contacts with large photovoltages.[21,37,38,67] This idea has been demonstrated in the photovoltaic community for Au/SiO_2/Si solar cells in which the VBO is larger than the CBO, leading to p-type systems achieving higher photovoltages than those with n-type semiconductors.[45] The model developed in this study predicts this trend. For example, **Figure 8A** shows that the performance of the p-type photoelectrode/catalyst is improved when the VBO is larger than the CBO; previous modeling efforts have not demonstrated this improved performance.[23,29,36,47] **Figure 8A** also shows the effect of independently varying the VBO (yellow to teal) and CBO (yellow to green) on MIS performance. Increasing the VBO enhances performance, as expected based on the result that p-type Au/SiO_2/Si solar cells outperform those of n-type.[45] Interestingly, increasing the CBO also improves photoelectrode performance, which is unexpected because the larger CBO increases the tunneling resistance of electrons. The combination of a high VBO and CBO (dark blue line) leads to the best MIS photoelectrode performance at 1.5 nm insulator thickness, demonstrating that a high symmetric band offset is superior to the previously proposed asymmetric band offsets.[21,37,38,67] This is the optimal band offset combination for photocathodes and photoanodes, as discussed in **Section S1**. This result is due to the large carrier concentrations at the semiconductor surface that increases the electron quasi-Fermi level, as discussed in the following paragraph. In other words, the electrons that tunnel into the metal carry more energy to drive the reaction when the VBO and CBO are both high.

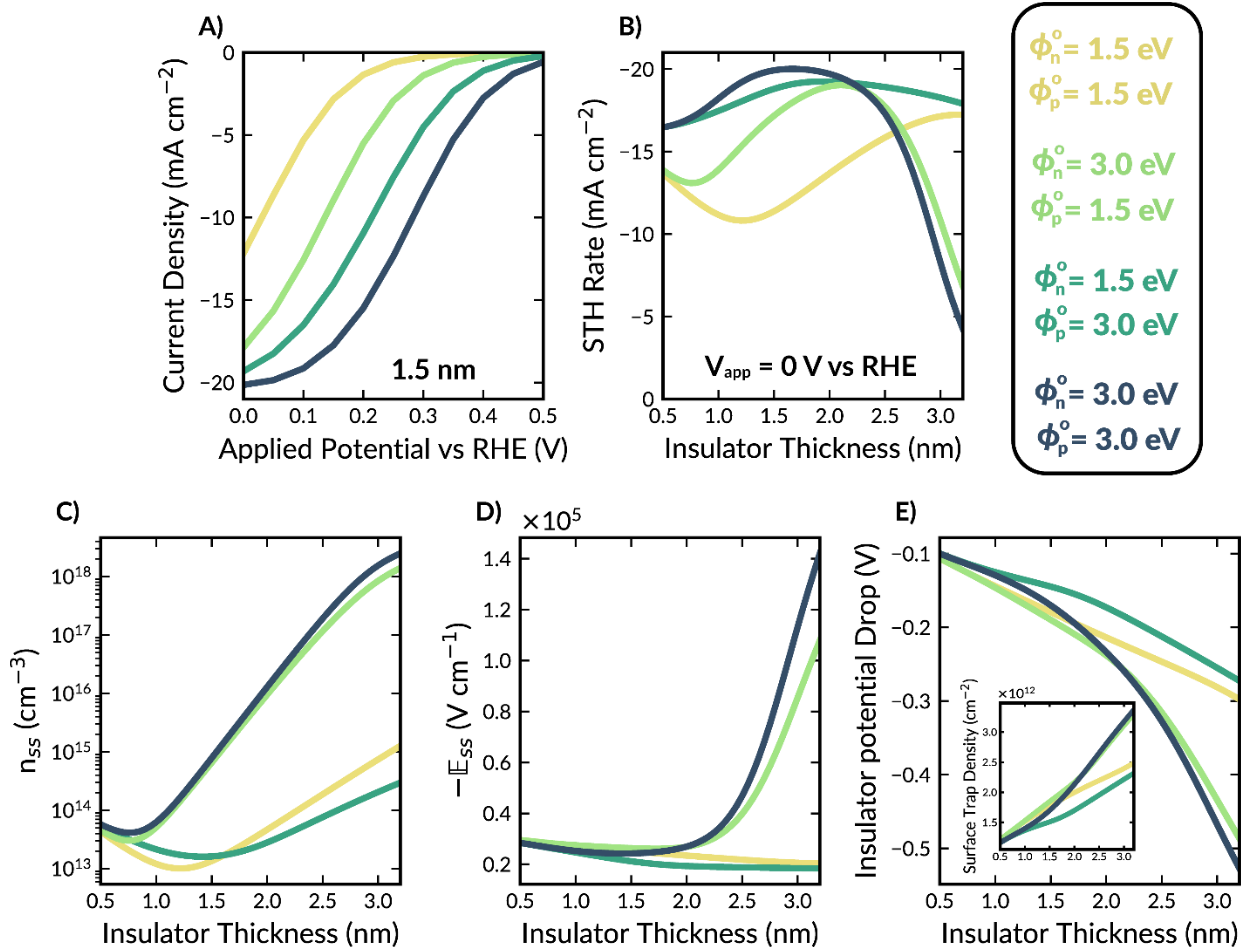

Figure 8: (A) Polarization curves for MIS photoelectrodes with high and low symmetric and asymmetric band offsets at 1.5 nm HfO_2. **(B)** Solar-to-H_2 (STH) rate, **(C)** interfacial electron concentration (n_s), **(D)** interfacial electric field (E_s), and **(E)** insulator potential drop (figure inset is surface trap density versus insulator thickness) as a function of insulator thickness at the reaction equilibrium potential (0 V vs RHE) for various band offset combinations.

Figure 8B shows that the dependence of the solar-to-H_2 (STH) rate on the insulator thickness changes considerably for different band offsets. In this instance, we use the STH rate at the reaction equilibrium potential (0 V vs RHE) as the performance metric, instead of the photovoltage at 0 mA cm^{-2}, as was done in the previous sections, because the STH rate is a direct measure of the ability of the photoelectrode to perform solar-to-chemical conversion. We note that the trends in photovoltage and STH rate with HfO_2 thickness are the same because of their relationship to E_{fn}^{ss} (**Figure S12**). A detailed discussion of the individual impact of the VBO and

CBO is provided in **Section S17** and **S18**, respectively. The MIS structure with a high VBO and CBO (dark blue line) exhibits the greatest STH rates at moderate HfO_2 thicknesses, but the STH rate is highly sensitive to thickness. By contrast, the high VBO and low CBO structure (teal line) does not reach as large of STH rates but is far less sensitive to HfO_2 thickness. This finding indicates that MIS photoelectrodes with a large VBO and CBO should use highly controlled insulator deposition methods, such as atomic layer deposition, to ensure the insulator has a low to moderate uniform thickness that is near its optimum value. Structures with a high majority carrier and low minority carrier band offset could be deposited by solution-based methods that exhibit lower insulator uniformity and thickness precision.[67]

The influence of varying band offsets on MIS performance can be understood by considering their effect on carrier concentration at the semiconductor surface, which ultimately influences bending in the electron quasi-Fermi level. A large VBO enhances the STH rate by causing holes to build up at the semiconductor surface, as a consequence of a large tunneling resistance. The high hole concentration helps to reduce the electric field and, consequently, increases the quasi-Fermi level of electrons; this, in turn, increases the overpotential for the reduction reaction. A large CBO results in a high electron tunneling resistance that leads to electron buildup at the semiconductor surface (see **Figure 8C**). The high electron concentration increases the electron quasi-Fermi level and, consequently, the reduction overpotential. Thus, a high VBO and CBO cause both carriers to build up at the semiconductor surface, which increases the electron quasi-Fermi level and enables operation closer to the flat-band potential. This phenomenon occurs at low to moderate insulator thicknesses because the carrier concentration is not high enough to cause significant carrier recombination.

Despite the large tunneling resistance with a high VBO and CBO, electrons tunnel at high rates because of the high electron concentration, except for when the insulating layer is thick. At large insulator thicknesses, MIS structures with a high CBO (teal and dark blue lines) experience a large reduction in the STH rate because of the overly large electron concentration at the semiconductor surface. This very high electron concentration increases the density of trapped electrons at the S/I interface, leading to a large insulator potential drop, and increases the magnitude of the electric field (see **Figure 8D, E)**. The high insulator potential drop and electric field reduces the quasi-Fermi level of electrons that tunnel into the metal and drive the HER process. These results not only reveal the optimal band offset combination for high STH rates and how it enhances performance but also helps to understand prior literature data (details are provided in **Sections S17** and **S18**).

3.5. Simulations of Alternative Insulating Materials

The importance of the VBO and CBO on MIS performance is further illustrated with simulations for insulating materials other than HfO_2. **Figure 9** shows the performance of MIS photoelectrodes in which BeO, HfO_2, and TiO_2 serve as the insulators; BeO and TiO_2 are chosen because they represent examples of large symmetric and asymmetric band offsets, respectively. Additional simulations of MIS structures involving MgO, SiO_2, ZrO_2, Al_2O_3, and Sc_2O_3 are shown in **Figure S15**. These materials were selected because of their large band offsets with Si or use in prior literature reports.[21] These simulations assume that the only properties that change are the VBO, CBO, insulator dielectric constant, and insulator effective mass and that all insulators have zero fixed charge, except HfO_2, because it depends on the deposition technique and precursors.[62] Although TiO_2 has been widely used as a protective insulating layer,[20,30,34,39] it does not result in the highest MIS performance. The low STH rate and photovoltage observed in this case are a result of the low CBO between Si and TiO_2, leading to a low electron concentration at the semiconductor

surface and, consequently, a low electron quasi-Fermi level. The highest STH rate and photovoltage are achieved using a ~0.8 nm BeO insulator, which is due to the high band offsets that create a large carrier concentration at the semiconductor surface. While, to the best of our knowledge, BeO has not been investigated as a protective insulator for MIS photoelectrodes, prior experimental work indicates that BeO should be stable over a large pH and potential window;[68] however, further efforts are required to confirm its stability in aqueous electrolytes. We note the STH rate and photovoltage are insensitive to insulator thicknesses for BeO and TiO_2 at ≳ 2 and ≳ 3 nm, respectively, because of the constant insulator potential drop. The potential drop is essentially constant because the rate of interfacial recombination has reached its saturation limit (*i.e.*, all the holes entering the S/I interface recombine) and, consequently, the density of filled trap states is constant.

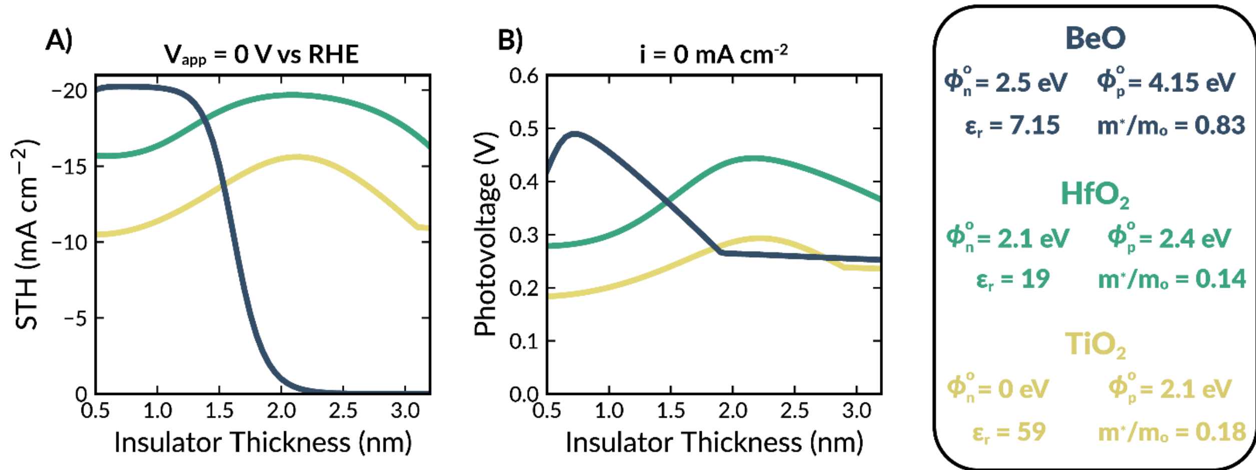

Figure 9: (A) Solar-to-H_2 (STH) rate and **(B)** photovoltage as a function of insulator thickness at 0 V vs RHE applied and 0 mA cm^{-2} current density, respectively.

The steep drop in performance of the MIS structure with BeO observed for thicknesses greater than 1.25 nm, seen in **Figure 9**, is due, in part, to its low dielectric constant. BeO does not effectively screen out the charge built up near the S/I interface, which results in a large insulator potential drop and the sharp decline in performance for thicknesses greater than the optimum.

Thus, it is desirable for insulators to have a high dielectric constant in addition to high band offsets. This criterion is the same as that for microelectronic applications,[69] although for photoelectrodes the insulator should be thin enough to allow current flow into the metal. Therefore, we can use the advances made in microelectronics research to improve MIS photoelectrode performance. Consequently, many novel binary and ternary metal-oxide materials with desirable properties identified through high-throughput computational screening might serve as next-generation insulators for photoelectrodes.[69] Moreover, bilayer insulators proposed for microelectronics may be useful as high dielectric insulator stacks with large band offsets for photoelectrodes.[70]

4. Summary

Metal-insulator-semiconductor (MIS) structures are a promising architecture for achieving highly active and stable photoelectrode/catalysts, a current challenge facing the field of artificial photosynthesis. Critical to their development is an understanding of how the insulator impacts MIS performance as well as identifying optimal insulator properties that enable selective carrier transport. This study presents a comprehensive theoretical model of an MIS photoelectrode, which is quantitatively validated by experimental current-voltage curves and photovoltage data as a function of insulator thickness. The model captures photon absorption and carrier generation, carrier and electrolyte transport, interfacial tunneling and kinetics, and nonidealities at the semiconductor/insulator (S/I) interface. Simulations based on this modeling framework revealed several important phenomena that enhance and/or limit the performance of MIS photoelectrodes. In particular, we identified that high carrier concentrations at the S/I interface reduce band bending and led to operation closer to the maximally attainable photovoltage, the flat-band potential. We demonstrated how these carrier concentrations are modified by the insulator properties (*i.e.*, thickness and band structure) through their effect on the carrier tunneling resistance. A large

buildup of carriers near the S/I interface is achieved with high S/I band offsets (conduction and valence band offsets) at low to moderate insulator thicknesses (*i.e.*, between 0.8 and 1.5 nm). With these properties, the resistance to carrier tunneling is high enough to cause significant carrier buildup but low enough to allow high minority carrier tunneling. Prospective insulating materials that exhibit high band offsets with Si are BeO, MgO, SiO_2, HfO_2, or ZrO_2. Simulations of these insulators in MIS photoelectrodes demonstrated their possible high performance and identified significant potential loss across the insulator at large thicknesses ($\gtrsim$ 1.5 nm). Therefore, controlled deposition techniques should be employed to ensure the insulator is uniform and has a low to moderate thickness. Future modeling efforts should account for nonideal interactions at high carrier concentrations, the effects of Fermi-level pinning of the semiconductor and interface trap states, and alternative interfacial transport mechanisms (*e.g.*, Fowler-Nordheim tunneling). Despite the neglect of these phenomena, the present model accurately replicated the experimental behavior of MIS photoelectrodes and offers critical insight into the future development of next-generation MIS structures.

Supporting Information

Translating between photocathode and photoanode; thermodynamics of photoanode; Tafel analysis; definition of metal catalyst potential; tunneling current derivation; linear fit of experimentally measured density of interface trap states versus insulator thickness; derivation of insulator potential drop; trap-assisted tunneling current density; derivation of ohmic contact boundary condition; convergence details; sources of error on photovoltage; insulator potential drop as a function of insulator thickness; full band diagram at open-circuit condition at various insulator thicknesses; interfacial transport rates vs insulator thickness; electron concentration versus HfO_2

thickness; photovoltage as a function of insulator thickness at no applied potential; impact of varying valence band offset; impact of varying conduction band offset; simulation of alternative insulators vs insulator thickness.

Acknowledgements

This material is based on work performed by the Liquid Sunlight Alliance, which is supported by the U.S. Department of Energy, Office of Science, Office of Basic Energy Sciences, Fuels from Sunlight Hub under Award Number DE-SC0021266. AJK acknowledges funding from the National Science Foundation Graduate Research Fellowship under Grant No. DGE 2146752. We also acknowledge Francesca Toma, Emily Warren, and Jason Cooper for fruitful discussions on semiconductor device physics.

Nomenclature

Roman

c	Speed of light (m s^{-1})
C	Interfacial capacitance (F m^{-2})
c_i	Concentration of species i (M)
C_n	Electron SRH recombination rate constant (cm^6 s^{-1})
C_p	Hole SRH recombination rate constant (cm^6 s^{-1})
C_{rad}	Direct radiative recombination rate constant (cm^3 s^{-1})
d	Insulator thickness (nm)
d_n	Thickness of charge build up at the semiconductor surface (nm)
D_i	Diffusivity of species i (m^2 s^{-1})
D_{it}	Density of interface trap states (m^{-2} eV^{-1})
$\mathbb{E}$	Electric field (V m^{-1})
E	Energy (eV)
E_g	Bandgap (eV)
F	Faraday constant (C mol^{-1})
f_t	Interface trap occupancy fraction
$G(x)$	Position dependent carrier generation rate (mol m^{-3} s^{-1})
g_D	Degeneracy factor

h	Planck's constant (m^2 kg s^{-1})
i	Current density (mA cm^{-2})
i_o^{HER}	Exchange current density for HER (mA cm^{-2})
$I(\lambda)$	Solar irradiance (W m^{-2})
k_B	Boltzmann constant (m^2 kg s^{-2} K^{-1})
K_n	Equilibrium constant in reaction n
k_n	Forward rate constant of reaction n
k_{-n}	Reverse rate constant of reaction n
$k_{n/p}$	Tunneling coefficient (mA cm mol^{-1})
L	Length (m)
m	Mass (kg)
n	Electron concentration (cm^{-3})
$N(\lambda)$	Incident photon flux (cm^{-2} s^{-1})
N_a^-	Acceptor-type doping density (mol m^{-3})
N_c	Effective density of states in conduction band (m^{-3})
N_d^+	Donor-type doping density (mol m^{-3})
n_e	Number of electrons transferred
n_i	Intrinsic carrier concentration (m^{-3})
N_i	Molar flux of species i (mol m^{-2} s^{-1})
N_t	Total number of interfacial trap sites (cm^{-2})
N_v	Effective density of states in valence band (m^{-3})
p	Hole concentration (cm^{-3})
P_T	Tunneling probability
q	Elementary charge (C)
Q	Charge density (C m^{-2})
R	Ideal-gas constant (J K^{-1} mol^{-1})
$R(\lambda)$	Reflectivity
R_i	Generation/consumption rate of species i (mol m^{-3} s^{-1})
s	Stoichiometric coefficient
T	Temperature (K)
U	Net generation rate in semiconductor (m^{-3} s^{-1})
U_o^{HER}	Standard state equilibrium potential for HER (V)
u_i	Mobility of species i (m^2 V^{-1} s^{-1})
V	Electric potential (V)
V_{fb}	Flat-band potential (V)
V_p	Difference in hole quasi-Fermi level and valence band (V)
V_{ph}	Photovoltage (V)
V_{sI}	Potential at the semiconductor-insulator interface without Δ (V)
x	1-dimensional position variable (m)
z_i	Charge of ion i

Greek

α	Reaction transfer coefficient
$\alpha(\lambda)$	Absorption coefficient (m^{-1})
$\alpha_{n/p}$	Electron or hole tunneling coefficient
Δ	Insulator potential drop (V)
$\Delta\phi$	Image force barrier lowering (V)
ε	Dielectric permittivity (F m^{-1})
ε_o	Permittivity of free space (F m^{-1})
η	Overpotential (V)
θ	Average capture cross-section (m^2)
λ	Wavelength (m)
ν_{th}	Thermal velocity (m s^{-1})
τ	Carrier lifetime (s)
ϕ_0	Neutral energy level (V)
ϕ_b	Schottky barrier (V)
$\phi_{n/p}$	Tunnel barrier (V)
φ	Fitted tunnel barrier adjustment (V)
χ	Electron affinity (eV)
ψ	Band bending (V)

Subscript

b	Boundary
bl	Boundary layer
c	Conduction band
cat	Metal catalyst / catalysis
eq	Equilibrium
f	Fermi
fix	Fixed
fm	Metal fermi
fn	Electron fermi
fp	Hole fermi
H_2	Hydrogen
H^+	Proton
I	Insulator
it	Interface trap
k	Reaction k
l	Liquid-phase
lim	Limiting
p	Holes
m	Metal
net	Sum of electron and hole

n	Electrons
ox	Native oxide
R	Recombination
ref	Reference
ss	Semiconductor surface
s	Semiconductor
v	Valence band
w	Water

Superscript

app	Applied
I	Insulator
o	Reference
oc	Ohmic contact
rad	Radiative
s	Semiconductor
SRH	Shockley-Reed-Hall
ss	Semiconductor surface

Acronyms

MS	Metal-Semiconductor
MIS	Metal-Insulator-Semiconductor
PV	Photovoltaic
PEC	Photoelectrochemical
S/I	Semiconductor-Insulator
STC	Solar-to-Chemical
STH	Solar-to-H_2
SRH	Shockley-Reed-Hall

References

(1) Bui, J. C.; Lees, E. W.; Pant, L. M.; Zenyuk, I. V.; Bell, A. T.; Weber, A. Z. Continuum Modeling of Porous Electrodes for Electrochemical Synthesis. *Chem. Rev.* **2022**, *122* (12), 11022–11084. https://doi.org/10.1021/acs.chemrev.1c00901.

(2) Schiffer, Z. J.; Manthiram, K. Electrification and Decarbonization of the Chemical Industry. *Joule* **2017**, *1* (1), 10–14. https://doi.org/10.1016/j.joule.2017.07.008.

(3) Sathre, R.; Scown, C. D.; Morrow, W. R.; Stevens, J. C.; Sharp, I. D.; Ager, J. W.; Walczak, K.; Houle, F. A.; Greenblatt, J. B. Life-Cycle Net Energy Assessment of Large-Scale Hydrogen Production via Photoelectrochemical Water Splitting. *Energy Environ. Sci.* **2014**, *7* (10), 3264–3278. https://doi.org/10.1039/c4ee01019a.

(4) Ager, J. W. *Semiconductor Light Absorbers*, 1st ed.; Sharp, I. D., Atwater, H. A., Lewerenz, H. J., Eds.; The Royal Society of Chemistry: London, 2019.

(5) Cheng, W. H.; Richter, M. H.; Sullivan, I.; Larson, D. M.; Xiang, C.; Brunschwig, B. S.; Atwater, H. A. CO_2 Reduction to CO with 19% Efficiency in a Solar-Driven Gas Diffusion Electrode Flow Cell under Outdoor Solar Illumination. *ACS Energy Lett.* **2020**, 470–476. https://doi.org/10.1021/acsenergylett.9b02576.

(6) Creissen, C. E.; Fontecave, M. Solar-Driven Electrochemical CO_2 Reduction with Heterogeneous Catalysts. *Adv. Energy Mater.* **2020**, *11* (43), 2002652. https://doi.org/10.1002/aenm.202002652.

(7) Chen, H.; Zheng, J.; Ballestas-barrientos, A.; Bing, J.; Liao, C.; Yuen, A. K. L.; Fois, C. A. M.; Valtchev, P.; Proschogo, N.; Bremner, S. P.; Atwater, H. A.; Boyer, C.; Maschmeyer, T.; Ho-baillie, A. W. Y. Solar-Driven Co-Production of Hydrogen and Value-Add Conductive Polyaniline Polymer. **2022**. https://doi.org/10.1002/adfm.202204807.

(8) He, J.; Janáky, C. Recent Advances in Solar-Driven Carbon Dioxide Conversion: Expectations versus Reality. *ACS Energy Lett.* **2020**, *5* (6), 1996–2014. https://doi.org/10.1021/acsenergylett.0c00645.

(9) Ager, J. W.; Shaner, M. R.; Walczak, K. A.; Sharp, I. D.; Ardo, S. Experimental Demonstrations of Spontaneous, Solar-Driven Photoelectrochemical Water Splitting. *Energy Environ. Sci.* **2015**, *8* (10), 2811–2824. https://doi.org/10.1039/c5ee00457h.

(10) Ben-Naim, M.; Aldridge, C. W.; Steiner, M. A.; Nielander, A. C.; Deustch, T. G.; Young, J. L.; Jaramillo, T. F. Demonstration of Photoreactor Platform for On-Sun Unassisted Photoelectrochemical Hydrogen Generation with Tandem III–V Photoelectrodes. *Chem Catal.* **2022**, *2* (1), 195–209. https://doi.org/10.1016/j.checat.2021.12.013.

(11) Ben-Naim, M.; Aldridge, C. W.; Steiner, M. A.; Britto, R. J.; Nielander, A. C.; King, L. A.; Deutsch, T. G.; Young, J. L.; Jaramillo, T. F. Engineering Surface Architectures for Improved Durability in III–V Photocathodes. *ACS Appl. Mater. Interfaces* **2021**, 1–8. https://doi.org/10.1021/acsami.1c18938.

(12) Zhang, Y.; Ye, C.; Duan, J.; Feng, H.; Liu, D.; Li, Q. Solar-Driven Carbon Dioxide

Reduction: A Fair Evaluation of Photovoltaic-Biased Photoelectrocatalysis and Photovoltaic-Powered Electrocatalysis. *Front. Energy Res.* **2022**, *10* (July), 1–8. https://doi.org/10.3389/fenrg.2022.956444.

(13) Chatterjee, P.; Ambati, M. S. K.; Chakraborty, A. K.; Chakrabortty, S.; Biring, S.; Ramakrishna, S.; Wong, T. K. S.; Kumar, A.; Lawaniya, R.; Dalapati, G. K. Photovoltaic/Photo-Electrocatalysis Integration for Green Hydrogen: A Review. *Energy Convers. Manag.* **2022**, *261* (April), 115648. https://doi.org/10.1016/j.enconman.2022.115648.

(14) Creel, E. B.; Corson, E. R.; Eichhorn, J.; Kostecki, R.; Urban, J. J.; McCloskey, B. D. Directing Selectivity of Electrochemical Carbon Dioxide Reduction Using Plasmonics. *ACS Energy Lett.* **2019**, *4* (5), 1098–1105. https://doi.org/10.1021/acsenergylett.9b00515.

(15) Schulte, L.; White, W.; Renna, L. A.; Ardo, S. Turning Water into a Protonic Diode and Solar Cell via Doping and Dye Sensitization. *Joule* **2021**, *5* (9), 2380–2394. https://doi.org/10.1016/j.joule.2021.06.016.

(16) Boutin, E.; Patel, M.; Kecsenovity, E.; Suter, S.; Janáky, C.; Haussener, S. Photo-Electrochemical Conversion of CO_2 Under Concentrated Sunlight Enables Combination of High Reaction Rate and Efficiency. *Adv. Energy Mater.* **2022**, *12* (30). https://doi.org/10.1002/aenm.202200585.

(17) Fujishima, A.; Honda, K. Electrochemical Photolysis of Water at a Semiconductor Electrode. *Nature* **1972**, *238* (5358), 37–38. https://doi.org/10.1038/238038a0.

(18) Hu, S.; Lewis, N. S.; Ager, J. W.; Yang, J.; McKone, J. R.; Strandwitz, N. C. Thin-Film Materials for the Protection of Semiconducting Photoelectrodes in Solar-Fuel Generators. *J. Phys. Chem. C* **2015**, *119* (43), 24201–24228. https://doi.org/10.1021/acs.jpcc.5b05976.

(19) Walter, M. G.; Warren, E. L.; McKone, J. R.; Boettcher, S. W.; Mi, Q.; Santori, E. A.; Lewis, N. S. Solar Water Splitting Cells. *Chem. Rev.* **2010**, *110* (11), 6446–6473. https://doi.org/10.1021/cr1002326.

(20) Seger, B.; Pedersen, T.; Laursen, A. B.; Vesborg, P. C. K.; Hansen, O.; Chorkendorff, I. Using TiO2 as a Conductive Protective Layer for Photocathodic H2 Evolution. *J. Am. Chem. Soc.* **2013**, *135* (3), 1057–1064. https://doi.org/10.1021/ja309523t.

(21) Hemmerling, J. R.; Mathur, A.; Linic, S. Design Principles for Efficient and Stable Water Splitting Photoelectrocatalysts. *Acc. Chem. Res.* **2021**, *54* (8), 1992–2002. https://doi.org/10.1021/acs.accounts.1c00072.

(22) Nakato, Y.; Ohnishi, T.; Tsubomura, H. Photo-Electrochemical Behaviors of Semiconductor Electrodes Coated with Thin Metal Films. *Chem. Lett.* **1975**, *53* (9), 883–886. https://doi.org/10.1017/CBO9781107415324.004.

(23) Quinn, J.; Hemmerling, J.; Linic, S. Guidelines for Optimizing the Performance of Metal-Insulator-Semiconductor (MIS) Photoelectrocatalytic Systems by Tuning the Insulator Thickness. *ACS Energy Lett.* **2019**, *4* (11), 2632–2638. https://doi.org/10.1021/acsenergylett.9b01609.

(24) Lieten, R. R.; Degroote, S.; Kuijk, M.; Borghs, G. Ohmic Contact Formation on N-Type

Ge. *Appl. Phys. Lett.* **2008**, *92* (2). https://doi.org/10.1063/1.2831918.

(25) Agrawal, A.; Shukla, N.; Ahmed, K.; Datta, S. A Unified Model for Insulator Selection to Form Ultra-Low Resistivity Metal-Insulator-Semiconductor Contacts to n-Si, n-Ge, and n-InGaAs. *Appl. Phys. Lett.* **2012**, *101* (4), 042108. https://doi.org/10.1063/1.4739784.

(26) Mönch, W. On the Alleviation of Fermi-Level Pinning by Ultrathin Insulator Layers in Schottky Contacts. *J. Appl. Phys.* **2012**, *111* (7), 073706. https://doi.org/10.1063/1.3699180.

(27) Contractor, A. Q.; Bockris, J. O. M. Investigation of a Protective Conducting Silica Film on N-Silicon. *Electrochim. Acta* **1984**, *29* (10), 1427–1434. https://doi.org/10.1016/0013-4686(84)87022-X.

(28) Scheuermann, A. G.; Lawrence, J. P.; Kemp, K. W.; Ito, T.; Walsh, A.; Chidsey, C. E. D.; Hurley, P. K.; McIntyre, P. C. Design Principles for Maximizing Photovoltage in Metal-Oxide-Protected Water-Splitting Photoanodes. *Nat. Mater.* **2016**, *15* (1), 99–105. https://doi.org/10.1038/nmat4451.

(29) Hemmerling, J.; Quinn, J.; Linic, S. Quantifying Losses and Assessing the Photovoltage Limits in Metal–Insulator–Semiconductor Water Splitting Systems. *Adv. Energy Mater.* **2020**, *10* (12), 1–10. https://doi.org/10.1002/aenm.201903354.

(30) Scheuermann, A. G.; Prange, J. D.; Gunji, M.; Chidsey, C. E. D.; McIntyre, P. C. Effects of Catalyst Material and Atomic Layer Deposited TiO_2 Oxide Thickness on the Water Oxidation Performance of Metal-Insulator-Silicon Anodes. *Energy Environ. Sci.* **2013**, *6* (8), 2487–2496. https://doi.org/10.1039/c3ee41178h.

(31) Cai, Q.; Hong, W.; Jian, C.; Li, J.; Liu, W. Insulator Layer Engineering toward Stable Si Photoanode for Efficient Water Oxidation. *ACS Catal.* **2018**, *8* (10), 9238–9244. https://doi.org/10.1021/acscatal.8b01398.

(32) Hemmerling, J. R.; Mathur, A.; Linic, S. Characterizing the Geometry and Quantifying the Impact of Nanoscopic Electrocatalyst/Semiconductor Interfaces under Solar Water Splitting Conditions. *Adv. Energy Mater.* **2022**, *12* (11), 1–10. https://doi.org/10.1002/aenm.202103798.

(33) Laskowski, F. A. L.; Nellist, M. R.; Venkatkarthick, R.; Boettcher, S. W. Junction Behavior of N-Si Photoanodes Protected by Thin Ni Elucidated from Dual Working Electrode Photoelectrochemistry. *Energy Environ. Sci.* **2017**, *10* (2), 570–579. https://doi.org/10.1039/c6ee03505a.

(34) Chen, Y. W.; Prange, J. D.; Dühnen, S.; Park, Y.; Gunji, M.; Chidsey, C. E. D.; McIntyre, P. C. Atomic Layer-Deposited Tunnel Oxide Stabilizes Silicon Photoanodes for Water Oxidation. *Nat. Mater.* **2011**, *10* (7), 539–544. https://doi.org/10.1038/nmat3047.

(35) Shen, X.; Yanagi, R.; Solanki, D.; Su, H.; Li, Z.; Xiang, C. X.; Hu, S. Comprehensive Evaluation for Protective Coatings: Optical, Electrical, Photoelectrochemical, and Spectroscopic Characterizations. *Front. Energy Res.* **2022**, *9* (January), 1–10. https://doi.org/10.3389/fenrg.2021.799776.

(36) Quinn, J.; Hemmerling, J.; Linic, S. Maximizing Solar Water Splitting Performance by

Nanoscopic Control of the Charge Carrier Fluxes across Semiconductor-Electrocatalyst Junctions. *ACS Catal.* **2018**, *8* (9), 8445–8552. https://doi.org/10.1021/acscatal.8b01929.

(37) Digdaya, I. A.; Trześniewski, B. J.; Adhyaksa, G. W. P.; Garnett, E. C.; Smith, W. A. General Considerations for Improving Photovoltage in Metal-Insulator-Semiconductor Photoanodes. *J. Phys. Chem. C* **2018**, *122* (10), 5462–5471. https://doi.org/10.1021/acs.jpcc.7b11747.

(38) Esposito, D. V.; Levin, I.; Moffat, T. P.; Talin, A. A. H2 Evolution at Si-Based Metal-Insulator-Semiconductor Photoelectrodes Enhanced by Inversion Channel Charge Collection and H Spillover. *Nat. Mater.* **2013**, *12* (6), 562–568. https://doi.org/10.1038/nmat3626.

(39) Gurudayal; Beeman, J. W.; Bullock, J.; Wang, H.; Eichhorn, J.; Towle, C.; Javey, A.; Toma, F. M.; Mathews, N.; Ager, J. W. Si Photocathode with Ag-Supported Dendritic Cu Catalyst for CO_2 Reduction. *Energy Environ. Sci.* **2019**, *12* (3), 1068–1077. https://doi.org/10.1039/c8ee03547d.

(40) Bae, D.; Seger, B.; Vesborg, P. C. K.; Hansen, O.; Chorkendorff, I. Strategies for Stable Water Splitting: Via Protected Photoelectrodes. *Chem. Soc. Rev.* **2017**, *46* (7), 1933–1954. https://doi.org/10.1039/c6cs00918b.

(41) Hu, S.; Shaner, M. R.; Beardslee, J. A.; Lichterman, M. F.; Brunschwig, B. S.; Lewis, N. S. Amorphous TiO_2 Coatings Stabilize Si, GaAs, and GaP Photoanodes for Efficient Water Oxidation. *Science (80-.).* **2014**, *344* (6187), 1005–1009. https://doi.org/10.1126/science.1251428.

(42) Hu, S.; Richter, M. H.; Lichterman, M. F.; Beardslee, J.; Mayer, T.; Brunschwig, B. S.; Lewis, N. S. Electrical, Photoelectrochemical, and Photoelectron Spectroscopic Investigation of the Interfacial Transport and Energetics of Amorphous TiO_2/Si Heterojunctions. *J. Phys. Chem. C* **2016**, *120* (6), 3117–3129. https://doi.org/10.1021/acs.jpcc.5b09121.

(43) King, A. J.; Bui, J. C.; Bell, A. T.; Weber, A. Z. Establishing the Role of Operating Potential and Mass Transfer in Multicarbon Product Generation for Photoelectrochemical CO_2 Reduction Cells Using a Cu Catalyst. *ACS Energy Lett.* **2022**, *7* (8), 2694–2700. https://doi.org/10.1021/acsenergylett.2c01041.

(44) Sze, S. M.; Ng, K. K. *Physics of Semiconductor Devices*, 3rd ed.; John Wiley: New York, 1981.

(45) Ng, K. K.; Card, H. C. Asymmetry in the SiO_2 Tunneling Barriers to Electrons and Holes. *J. Appl. Phys.* **1980**, *51* (4), 2153–2157. https://doi.org/10.1063/1.327888.

(46) Green, M. A.; King, F. D.; Shewchun, J. Minority Carrier MIS Tunnel Diodes and Their Application to Electron- and Photo-Voltaic Energy Conversion-I. Theory. *Solid State Electron.* **1974**, *17* (6), 551–561. https://doi.org/10.1016/0038-1101(74)90172-5.

(47) Card, H. C. Photovoltaic Properties of MIS-Schottky Barriers. *Solid State Electron.* **1977**, *20* (12), 971–976. https://doi.org/10.1016/0038-1101(77)90206-4.

(48) Newman, J.; Thomas-Alyea, K. E. *Electrochemical Systems*, 3rd ed.; Wiley-Interscience:

Hoboken, 2004.

(49) Card, H. C.; Rhoderick, E. H. Studies of Tunnel MOS Diodes I. Interface Effects in Silicon Schottky Diodes. *J. Phys. D. Appl. Phys.* **1971**, *4* (10), 1589–1601. https://doi.org/10.1088/0022-3727/4/10/319.

(50) Olsen, L. C. Model Calculations for Metal-Insulator-Semiconductor Solar Cells. *Solid State Electron.* **1977**, *20* (9), 741–751. https://doi.org/10.1016/0038-1101(77)90002-8.

(51) Green, M. A.; Shewchun, J. Current Multiplication in Metal-Insulator-Semiconductor (MIS) Tunnel Diodes. *Solid State Electron.* **1974**, *17* (4), 349–365. https://doi.org/10.1016/0038-1101(74)90127-0.

(52) Green, M. A.; Keevers, M. J. Optical Properties of Intrinsic Silicon at 300 K. *Prog. Photovoltaics Res. Appl.* **1995**, *3* (3), 189–192. https://doi.org/10.1002/pip.4670030303.

(53) PV Lighthouse https://www.pvlighthouse.com.au/.

(54) Ferguson, D. C.; Wilt, D. M.; Hepp, A. F.; Kolecki, J. C.; Siebert, M. W.; Jenkins, P. P.; Scheiman, D. A.; Fatemi, N. S.; Hoffman, R. W. The Mars Pathfinder Wheel Abrasion Experiment. *Mater. Des.* **2001**, *22* (7), 555–564. https://doi.org/10.1016/S0261-3069(01)00016-4.

(55) Ehlinger, V. M.; Crothers, A. R.; Kusoglu, A.; Weber, A. Z. Modeling Proton-Exchange-Membrane Fuel Cell Performance/Degradation Tradeoffs with Chemical Scavengers. *J. Phys. Energy* **2020**, *in press*. https://doi.org/https://doi.org/10.1088/2515-7655/abb194.

(56) Bui, J. C.; Kim, C.; Weber, A. Z.; Bell, A. T. Dynamic Boundary Layer Simulation of Pulsed CO_2 Electrolysis on a Copper Catalyst. *ACS Energy Lett.* **2021**, *6* (4), 1181–1188. https://doi.org/10.1021/acsenergylett.1c00364.

(57) Afanas'ev, V. V.; Stesmans, A.; Chen, F.; Shi, X.; Campbell, S. A. Internal Photoemission of Electrons and Holes from (100)Si into HfO_2. *Appl. Phys. Lett.* **2002**, *81* (6), 1053–1055. https://doi.org/10.1063/1.1495088.

(58) Martens, K.; Wang, W. F.; Dimoulas, A.; Borghs, G.; Meuris, M.; Groeseneken, G.; Maes, H. E. Determining Weak Fermi-Level Pinning in MOS Devices by Conductance and Capacitance Analysis and Application to GaAs MOS Devices. *Solid. State. Electron.* **2007**, *51* (8), 1101–1108. https://doi.org/10.1016/j.sse.2007.06.002.

(59) Qi, F.; Yang, Z.; Zhang, J.; Wang, Y.; Qiu, Q.; Li, H. Interfacial Reaction-Induced Defect Engineering: Enhanced Visible and Near-Infrared Absorption of Wide Band Gap Metal Oxides with Abundant Oxygen Vacancies. *ACS Appl. Mater. Interfaces* **2020**, *12* (49), 55417–55425. https://doi.org/10.1021/acsami.0c16543.

(60) Triyoso, D. H.; Hegde, R. I.; Zollner, S.; Ramon, M. E.; Kalpat, S.; Gregory, R.; Wang, X. D.; Jiang, J.; Raymond, M.; Rai, R.; Werho, D.; Roan, D.; White, B. E.; Tobin, P. J. Impact of Titanium Addition on Film Characteristics of HfO_2 Gate Dielectrics Deposited by Atomic Layer Deposition. *J. Appl. Phys.* **2005**, *98* (5). https://doi.org/10.1063/1.2030407.

(61) COMSOL Multiphysics Semiconductor Module.

(62) Sreenivasan, R.; McIntyre, P. C.; Kim, H.; Saraswat, K. C. Effect of Impurities on the Fixed Charge of Nanoscale HfO_2 Films Grown by Atomic Layer Deposition. *Appl. Phys. Lett.* **2006**, *89* (11), 1–4. https://doi.org/10.1063/1.2348735.

(63) Monaghan, S.; Hurley, P. K.; Cherkaoui, K.; Negara, M. A.; Schenk, A. Determination of Electron Effective Mass and Electron Affinity in HfO_2 Using MOS and MOSFET Structures. *Solid. State. Electron.* **2009**, *53* (4), 438–444. https://doi.org/10.1016/j.sse.2008.09.018.

(64) Han, J. P.; Vogel, E. M.; Gusev, E. P.; D'Emic, C.; Richter, C. A.; Heh, D. W.; Suehle, J. S. Energy Distribution of Interface Traps in High-K Gated MOSFETs. *Dig. Tech. Pap. - Symp. VLSI Technol.* **2003**, 161–162. https://doi.org/10.1109/vlsit.2003.1221135.

(65) Adam, J.; Rogers, M. D. The Crystal Structure of ZrO_2 and HfO_2. *Acta Crystallogr.* **1959**, *12* (11), 951–951. https://doi.org/10.1107/s0365110x59002742.

(66) Shen, X.; Zhao, T.; Su, H.; Yang, M.; Chen, J.; Liu, Y.; Yanagi, R.; Solanki, D.; Hu, S. Tuning Intermediate Bands of Protective Coatings to Reach the Bulk-Recombination Limit of Stable Water-Oxidation GaP Photoanodes. *Adv. Energy Mater.* **2022**, *12* (29). https://doi.org/10.1002/aenm.202201314.

(67) Kast, M. G.; Enman, L. J.; Gurnon, N. J.; Nadarajah, A.; Boettcher, S. W. Solution-Deposited F:SnO_2/TiO_2 as a Base-Stable Protective Layer and Antireflective Coating for Microtextured Buried-Junction H_2-Evolving Si Photocathodes. *ACS Appl. Mater. Interfaces* **2014**, *6* (24), 22830–22837. https://doi.org/10.1021/am506999p.

(68) Gulbrandsen, E.; Johansen, A. M. J. A Study of the Passive Behaviour of Beryllium in Aqueous Solutions. *Corros. Sci.* **1994**, *36* (9), 1523–1531. https://doi.org/10.1016/0010-938X(94)90050-7.

(69) Yim, K.; Yong, Y.; Lee, J.; Lee, K.; Nahm, H. H.; Yoo, J.; Lee, C.; Hwang, C. S.; Han, S. Novel High-K Dielectrics for next-Generation Electronic Devices Screened by Automated Ab Initio Calculations. *NPG Asia Mater.* **2015**, *7* (6), 1–6. https://doi.org/10.1038/am.2015.57.

(70) Vaziri, S.; Belete, M.; Dentoni Litta, E.; Smith, A. D.; Lupina, G.; Lemme, M. C.; Östling, M. Bilayer Insulator Tunnel Barriers for Graphene-Based Vertical Hot-Electron Transistors. *Nanoscale* **2015**, *7* (30), 13096–13104. https://doi.org/10.1039/c5nr03002a.

For Table of Contents Only